Restoration of mitochondrial complex III function in hepatocytes highlights the liver as a key thermogenic organ independent of brown adipocyte activation

Rishi Banerjee[1,2], Divya Upadhyay[1,2], Tomas Zarybnicky[2], Satu Kuure[2,3], Vineta Fellman[1,2,5,6], Janne Purhonen[1,2,4], and Jukka Kallijärvi[1,2*]

[1]Folkhälsan Research Center, Helsinki, Finland

[2]Stem Cells and Metabolism Research Program, Faculty of Medicine, University of Helsinki, Finland

[3]GM-unit, Laboratory Animal Center, Helsinki Institute of Life Science, University of Helsinki, Finland

[4]Department of Laboratory Medicine, Karolinska Institutet, Huddinge, Sweden

[5]Children's Hospital, University of Helsinki, Finland

[6]Department of Clinical Sciences Lund, Pediatrics, Lund University, Sweden

[*]Corresponding author (jukka.kallijarvi@helsinki.fi)

Abstract

The liver is the key hub of systemic energy metabolism and growth, yet it is surprisingly rarely a major affected organ in mitochondrial diseases that compromise oxidative phosphorylation. *Bcs1l*$^{p.S78G}$ knock-in mice, carrying a respiratory complex III (CIII)-deficiency patient mutation, present juvenile-onset liver and kidney disease, growth restriction, lipodystrophy and premature death. To explore the as yet poorly understood systemic metabolic roles of the liver in mitochondrial diseases, we utilized this model and performed recombinant adeno-associated viruses (rAAV)-based gene therapy using a hepatocyte-specific promoter to drive wild-type BCS1L expression. A single rAAV-*Bcs1l* intraperitoneal injection into presymptomatic 3-week-old mice transduced the liver, restored hepatocyte CIII assembly and activity, prevented liver disease and was sufficient to improve growth, prevent lethal hypoglycemia, and extend survival by 100%. Unexpectedly, the hepatocyte-specific gene replacement also prevented severe hypothermia. Mechanistically, the mutant mice lacked signs of thermogenic BAT activation and thermoneutral housing did not correct the hypothermia. The mice exhibited impaired thermosensation, implying failure to respond to hypothermic cues. Immunostaining revealed grossly abnormal foot pad innervation, suggesting sensory neuropathy and impaired thermosensing. The rAAV-*Bcs1l*-treated mice maintained near-normal body temperature without induction of BAT thermogenesis, demonstrating that mitochondrial respiration in hepatocytes is both essential and sufficient for euthermia in juvenile mice. These findings emphasize the crucial role of the liver in thermoregulation, suggest sensory neuropathy as an unexpected cause of hypothermia, and demonstrate the therapeutic potential of tissue-specific gene therapy in a preclinical model of a multiorgan mitochondrial disease.

Introduction

Mitochondrial diseases are a heterogeneous group of monogenic inherited errors of metabolisms, which typically affect - directly or indirectly - oxidative phosphorylation (OXPHOS). They can manifest in almost any tissue of the body, often with ambiguous genotype-phenotype correlation[1]. Many aspects of interorgan communication between the affected and non-affected organs in mitochondrial diseases are poorly understood[2,3]. Mitochondrial diseases lack effective treatments and their clinical management relies on supportive care[4]. Preclinical gene therapy, or gene replacement therapy, studies[5] are still limited but some have shown that organ-specific gene therapy can ameliorate both cell autonomous and systemic phenotypes. These include mouse models of dominant optic atrophy[6], Barth syndrome[7], Friedreich ataxia[8], MPV17-related disease[9], mitochondrial neurogastrointestinal encephalopathysyndrome[10], Leigh syndrome[11,12], ethylmalonic encephalopathy[13], and autosomal recessive human thymidine kinase 2 deficiency[14]. Recombinant adeno-associated viruses (rAAVs) are widely utilized delivery vectors of DNA in gene therapy strategies, partially due to their safety, being non-integrating viruses[15]

Complex III (CIII) deficiencies[16] are a subgroup of mitochondrial diseases, GRACILE syndrome (fetal-onset **g**rowth **r**estriction, **a**minoaciduria, **c**holestasis, liver **i**ron overload, **l**actic acidosis, and **e**arly death during infancy) being one of the most severe phenotypes[17,18]. *Bcs1l*$^{p.S78G}$ knock-in mice, carrying the GRACILE syndrome patient mutation, recapitulate most of the clinical manifestations[19–21]. On an *mt-Cyb*$^{p.D254N}$ mtDNA background that exacerbates the CIII deficiency, the homozygotes succumb to metabolic crisis by 4-5 weeks of age[19,22]. The liver is one of the main affected organs in GRACILE syndrome patients and in the *Bcs1l*$^{p.S78G}$ mice. However, it is unknown to which degree the systemic metabolic phenotypes like growth restriction, lipodystrophy, and hypoglycemia are liver-dependent in this model[23]. The liver is particularly amenable to viral transduction by rAAVs in mice[24]. To probe the roles of the liver in the systemic energy deficiency in OXPHOS dysfunction and as a target tissue for gene therapy, we utilized rAAVs expressing wild-type mouse *Bcs1l* under a broad or a hepatocyte-specific[25] promoter to restore CIII function and OXPHOS in the *Bcs1l*$^{p.S78G}$ mice. As outcomes, we assessed growth, liver disease progression, energy metabolism, body temperature and survival. We show that the hepatocyte-specific rescue was sufficient to fully prevent the liver disease and ameliorate systemic manifestations, resulting in doubling of the survival. We found that the CIII deficient mice are hypothermic and apparently fail to activate brown adipose tissue (BAT) thermogenesis. Unexpectedly, restoration of CIII

function in hepatocytes was sufficient to normalize their body temperature without an effect on BAT activation markers.

Results

Restoration of CIII function in hepatocytes doubles the survival of mutant mice

We injected presymptomatic (P19-23) mutant mice (genotype *Bcs1l*$^{p.S78}$;*mt-Cyb*$^{p.D254N}$, referred to as mutant from now on) with rAAV, serotype 9, assessed disease progression and performed autopsy according to the experimental setup and timeline shown in Fig. 1A and B. Hepatocyte-specific ApoE enhancer and α1-antitrypsin (AAT) promoter[26] drove mouse BCS1L expression. As a control, we injected the same rAAV backbone expressing EGFP. The groups of mutant mice injected with rAAV carrying the *Bcs1l* or *EGFP* transgene will be referred to as AAT-*Bcs1l* and AAT-*EGFP*, respectively. Fluorescence microscopy of an AAT-*EGFP* injected liver (Supplementary Fig. 1A) demonstrated high transduction efficiency similar to previously published results[26]. The mutant liver that had received AAT-*Bcs1l* appeared visually as healthy as the WT liver (Supplementary Fig. 1B). qPCR analysis for total and virally-expressed *Bcs1l* at P28 confirmed viral expression of *Bcs1l*, which resulted in approximately 20-fold increased total *Bcs1l* mRNA in the liver (Fig. 1C). As a third group, to ensure persistent expression in the growing liver, we co-injected PiggyBac transposase-encoding rAAVs. As a control for hepatocyte-specific effects we used a construct with the broadly active CAG promoter (CAG-*Bcs1l*).

The mutants injected with AAT-*Bcs1l* showed no signs of the terminal deterioration, which consistently appeared in the AAT-*EGFP*-injected control group by the age of one month, and their median survival was doubled to 58 days (Fig. 1D). *Bcs1l* expression was ~2.4 fold higher compared to WTs at the end stage (Fig. 1E). Inclusion of a transposase-expressing virus to allow genomic intergration resulted in significantly higher end stage hepatic *Bcs1l* expression (Fig. 1E), but the survival did not extend further (Fig. 1D). This suggests that the eventual deterioration in the liver-targeted group was due to the disease progression in the other affected organs. Broader *Bcs1l* expression driven by the CAG promoter did increase the survival further, albeit relatively modestly (15%), to a median of 66 days (Fig. 1D), and the end stage hepatic expression of *Bcs1l* was higher than with the hepatocyte-specific vector (without transposase-meadiated genomic intergration) (Fig. 1E). At P28, AAT-*Bcs1l* significantly improved the low mean blood glucose, and, importantly, none of the treated mice showed blood glucose less than

<2.5mmol/L (Fig. 1F), avoiding the lethal metabolic crisis[23,27,28]. At the end stage (P53-60), the glucose concentrations dropped again, even to less than <2.5mmol/L (Fig. 1F). While the control mutants started to lose weight after P25, the mutants treated with AAT-*Bcs1l* were able grow (Fig. 1G) and maintained hepatic insulin-like growth factor 1 (*Igf1*) and growth hormone receptor (*Ghr*) expression (Fig. 1H and I).

Restoration of CIII function in hepatocytes prevents hepatopathy and supports kidney tubular cells

We isolated mitochondria from the liver and performed blue native gel electrophoresis (BNGE) to assess restoration of CIII assembly by the AAT-*Bcs1l*. As shown previously[20], the mutant mitochondria showed a greatly diminished amount of fully assembled CIII dimer ($CIII_2$) based on the presence of UQCRFS1 (RISP). Almost all of the residual fully-assembled $CIII_2$ was in the CI-$CIII_2$ supercomplexes (SC), with free $CIII_2$ being absent. The gene therapy efficiently restored the levels of fully-assembled $CIII_2$ (Fig. 2A). In isolated mutant liver mitochondria, the mean CIII activity was around 26% of WT and the gene therapy increased the CIII activity to approximately 74% of WT (Fig. 2B). Along with the restored CIII activity, the gene therapy also improved the hepatic ATP levels (Fig. 2C). Our previous data showed compensatory mitochondrial biogenesis in the *Bcs1l*$^{p.S78G}$ mouse tissues[29]. Here, the mitochondrial biogenesis marker *Ppargc1a* (*Pgc-1α*) tended to be normalized by AAT-*Bcs1l* (Fig. 2D) and the mitochondrial mass markers VDAC1 and HSP60 were at WT lever in the AAT-*Bcs1l*-injected mice (Fig. 2E). HSP60 immunostaining of mitochondria in liver tissue sections showed an abnormal pattern of mitochondria in the mutant hepatocytes, which was again fully prevented by AAT-*Bcs1l* (Supplementary Fig. 1D).

Histopathological analysis of the P28 mutant mice showed early-stage hepatopathy characterized by expansion of portal areas, increase in ductular reactions, microvesicular fat accumulation and loss of glycogen (Fig. 3A-C and E) and cell death (Fig. 3D and F). The AAT-*Bcs1l* fully prevented these changes at P28 (Fig. 3A-F and supplementary Fig 2A-E), as well as the upregulation of the disease marker gene[30] glutathione S-transferase 1 (*Gsta1*) at P28 (Fig 3G). In addition, AAT-*Bcs1l* normalized the expression of the mitochondrial dysfunction-associated mitokine, growth-differentiation factor 15 (*Gdf15*) (Fig. 3H). The hepatic ductular reactions, and *Gsta1* and *Gdf15* expression were upregulated again at the end stage of survival (Supplementary Fig. 2D, F and G), demonstrating the significant impact of AAT-*Bcs1l* in delaying liver disease. Mechanistically, the *Bcs1l*$^{p.S78G}$ mice show c-MYC-driven hepatocyte

proliferation, leading to DNA damage, cell cycle arrest and cellular senescence due to depletion of biosynthetic resources[21]. AAT-*Bcs1l* partially prevented the hepatic DNA damage based on γH2AX quantification (Fig. 4A), and fully prevented the upregulation of the cell cycle arrest marker CDKN1A (Fig. 4B) and that of c-MYC (Fig. 4C). AAT-*Bcs1l* tended to decrease the cell proliferation markers PCNA and cyclin A2 below wild-type level (Fig. 4D). Finally, upregulation of the senescence markers cathepsin L (*Ctsl*) and *Gpnmb* was fully prevented by AAT-*Bcs1l* at P28 (Fig. 4E and F, Supplementary Fig. 2H-I).

Kidney tubulopathy, presumably due to damage to the mitochondria-rich proximal tubular epithelial cells, is another prominent phenotype in GRACILE syndrome patients and in the mutant mice[17,19,20]. This results in increased cell death and loss of cortex volume already at P28 (Supplementary Fig. 3A-D). Surprisingly, despite that the number of apoptotic cells was not decreased (Supplementary Fig. 3B and D), the kidney cortex thickness was slightly increased by AAT-*Bcs1l* (Supplementary Fig. 3A and C), suggesting a systemic effect from the rescued liver. Interestingly, kidney cortex thickness was at wild-type level even in the end-stage samples from the group co-injected with PiggyBac transposase virus and CAG-*Bcs1l* injected mice (Supplementary Fig. 3E-J). In contrast, albuminuria, a typical consequence of glomerular dysfunction[31], was not affected by the gene therapy (Supplementary Fig. 3K and L).

CIII-deficient mice are hypothermic and show loss of thermosensation

During manual handling of the mutant mice, we observed that they were cold. Skin temperature readings showed that the symptomatic (>P25) mutant mice are hypothermic with a mean skin temperature of 31.0ºC and estimated core temperature of 35.0ºC (range 32-36ºC). Unexpectedly, the body temperature was completely normalized by AAT-*Bcs1l* (Fig. 5A and B). The gene therapy also prevented the upregulation of the cold inducible genes RNA-binding motif protein 3 (*Rbm3*) and cold-inducible RNA-binding protein variant 4 (*Cirbp4*) (Fig. 5C), indicating a transcriptional response to hypothermia. The mean core temperature dropped again to 31ºC at the end stage of the treated mice (Supplementary Fig. 4A and B), indicating its key role as a pathomechanism.

Thyroid hormones stimulate thermogenesis mainly by increasing basal metabolism, but also exert direct effects on BAT[32,33]. We measured plasma levels of T3 and T4 and found that they were similar in wild-type and mutant mice (Supplementary Fig. 4C), ruling out hypothyroidemia as a cause for the hypothermia. To further explore thyroid hormone-related basal thermogenesis, we injected the mice with T3 on four consecutive days before sacrificing.

T3 did not increase the body temperature but dramatically decreased it, indicating that stimulating basal metabolism against OXPHOS deficiency was harmful (Supplementary Fig. 4D). Leptin, a hormone released by white adipose tissue (WAT), acts as another essential messenger in energy sensing, transmits information about peripheral fat reserves to the hypothalamus, and can contribute to thermoregulation via pyrexia[34,35]. Both GRACILE syndrome patients and *Bcs1l*$^{p.S78G}$ mice show severe loss of WAT mass, likely a consequence of their starvation-like metabolic stress[20,23]. Mean plasma leptin was ~75 pg/ml in WT mice at age P115 but barely detectable in the mutant mice (Supplementary Fig. 4E). In the juvenile mice, plasma leptin is naturally very low and was below detection limit in all mice, preventing the assessment of the potential effect of gene therapy. However, at P28 rAAV-*Bcs1l* slightly increased the fat mass, with which leptin expression correlates, in females (Supplementary Fig. 4F).

The *Bcs1l*$^{p.S78G}$ mice are small and lack dermal adipose tissue[21] and may therefore be more prone to heat loss under the standard housing temperature. To interrogate this, we housed a group of *Bcs1l*$^{p.S78G}$ mice at 30-32ºC for 10 days and measured their skin and core temperature at P33. Surprisingly, the hypothermia was not corrected by the thermoneutral housing but even slightly exacerbated (Fig. 5D). Suspecting defective thermosensation, we inspected hot plate response data from young adult mice. This indicated compromised nociception (Fig. 5E), raising the possibility that sensory neuropathy may be responsible for their reduced responsiveness to external temperature cues. Adult *Bcs1l*$^{p.S78G}$ mice also showed reduced hearing sensitivity, a manifestation of sensory neuropathy (Supplementary Fig. 4G). We performed immunofluorescent labelling of peripheral nerves in the hind limb foot pad to assess the integrity of the sensory nervous system. The mutant foot pads exhibited fragmented β3 tubulin (TUJ1, pan-neuronal marker) labelling and minimal Calcitonin gene-related peptide (CGRP, sensory neuron marker), neurofilament M (NF-M) and neurofilament H (NF-H) signals at the epidermal/dermal boundary of the foot pad (Fig. 5F and Supplementary Fig. 4H). These data indicate severe peripheral neuropathy, which may lead to retarded thermosensation.

Hepatocyte-specific restoration of CIII activity maintains euthermia independent of BAT

A highly innervated organ, BAT undergoes thermogenesis-promoting remodeling in response to neuronal cold signals from the hypothalamus. In contrast to the neuronal markers in foot pads, tyrosine hydroxylase (TH), a marker for sympathetic nerve terminals, was not decreased in the mutant BAT (Fig. 6A). When activated by hypothalamic signals, these nerves release

noradrenaline, which binds to β3 adrenergic receptors (ADRB3) on adipocytes, stimulating BAT thermogenesis to counteract cold[36,37]. Suprisingly, *Adrb3* mRNA was downregulated by ~90% in the BAT of the mutant mice (Fig. 6B), which strongly suggests decreased adrenergic signaling to BAT despite the hypothermia. ADRB3 has been shown to be downregulated after persistent adrenergic stimulation and this appears to be mediated via TRIB1 (Tribbles pseudokinase 1) upregulation[38]. However, *Trib1* expression was downregulated in the mutant BAT (Supplementary Fig. 5A), suggesting that adrenergic overstimulation was not the cause of the reduced *Adrb3* expression. Astonishingly, *Adrb3* expression remained suppressed in the AAT-*Bcs1l*-injected mice (Fig. 6B), indicating that the normalization of their core temperature did not depend on BAT adrenergic stimulation.

Uncoupling, the process by which uncoupling protein 1 (UCP1) dissipitates the mitochondrial membrane potential by allowing proton flow, is the key heat-producing mechanism in BAT[39]. In line with the *Adrb3* downregulation, UCP1 protein was unchanged and *Ucp1* mRNA tended to be even slightly downregulated in the mutant BAT (Fig. 6C and D). Also the expression of the thermogenic marker *Dio2*, which catalyzes the conversion of T4 to T3 in BAT, was unchanged (Fig. 6E), whereas the brown adipocyte markers *Cidea* and *Prdm16* were downregulated in the mutant BAT (Fig. 6F and G). AAT-*Bcs1l* had no effect on *Cidea* (Fig. 6F) and only slight effect on *Prdm16* (Fig. G) . The transcriptional regulator *Ppargc1a* (*Pgc-1α*), a driver of mitochondrial biogenesis in BAT thermogenesis[37], was slightly upregulated in the mutant BAT (Fig. 6H), but markers of mitochondrial mass, HSP60 and SDHA, were unaffected (Fig. 6I). These data further support the interpretation that BAT thermogenesis was not activated in the *Bcs1l*$^{p.S78G}$ mice at normal housing temperature.

Skeletal muscle is a major adaptive thermogenic organ, mediating shivering (muscle contraction) and non-shivering thermogenesis that may be affected by the low skeletal muscle CIII activity in the *Bcs1l*$^{p.S78G}$ mice[22]. Sarcolipin (SLN)-mediated uncoupling of the SERCA Ca^{2+} pump is considered the prime mechanism of non-shivering thermogenesis in the skeletal muscle[40]. At P28, expression of *Sln* in the quadriceps was increased (Fig. 6J). To aid thermogenesis, SLN also promotes mitochondrial biogenesis and oxidative energy metabolism in skeletal muscle via *Pgc-1α*[41,42]. *Pgc-1α* was indeed induced in the mutant skeletal muscle (Fig. 6K), but on the basis of respiratory subunit *Ndufs3* (CI) and *Sdhb* (CII) expression mitochondrial mass was unchanged between the groups (Fig. 6L). However, *Pdk4* and *Cd36* expression were robustly upregulated (Fig. 6M and N) indicating a metabolic shift from carbohydrate to lipid utilization in the mutant muscle upon glycogen depletion. Strikingly, the

upregulation of *Pdk4* and *Cd36* in skeletal muscle was prevented by AAT-*Bcs1l* (Fig. 6M and N), indicating a stong metabolic contribution from the liver to skeletal muscle fuel use.

The liver, being the master coordinator of systemic fuel mobilization and utilization, provides other organs with glucose from glycogenolysis and gluconeogenesis, and ketone bodies from fatty acid oxidation during fasting in wild-type animals and in the chronic fasting-like condition of the *Bcs1l*$^{p.S78G}$ mice[23,28]. In the mutant liver, the expression of pyruvate dehydrogenase kinase 4 (*Pdk4*), which phosphorylates and inactivates the pyruvate dehydrogenase complex to dampen glucose utilization, was highly increased, in line with the hypoglycemia (Fig. 6O). Conversely, reflecting the the hepatic fat accumulation (Fig. 3B), the fatty acid uptake receptor *Cd36* was upregulated (Fig 6P). However, the expression of *Pparα*, a major driver of fatty acid oxidation (Fig 6Q) and *Hadhb*, which catalyzes the final stage of β-oxidation, were significantly decreased (Fig 6R), as was carnitine palmitoyl transferase 1a (*Cpt1a*) (Fig 6S), which controls the entry and oxidation of long chain fatty acid in the mitochondria. In the mutant liver, phosphorylation of AMP-dependent protein kinases (AMPK), a cellular sensor of ATP and glucose availability[21,43], was increased (Fig 6T). These transcriptional and protein-level fuel utilization markers were fully normalized by AAT-*Bcs1l* which, together with the restored glycogen stores and resolution of the the fat accumulation, indicates restoration of hepatic glucose metabolism and β-oxidation until the end stage (Supplementary Fig 5C-E). Taken together, the data from BAT, skeletal muscle and liver demonstrate the key role of basal liver metabolism as necessary and sufficient to maintain body temperature in the CIII-deficient juvenile mice.

Discussion

With a straightforward preclinical trial strategy as starting point, we show that a single i.p. injection of hepatocyte-specific rAAV-*Bcs1l* into juvenile pre-symptomatic CIII-deficient mutant mice prevents liver disease, improves growth, corrects hypothermia, and doubles the survival. The immediate cause of the extended survival was likely the prevention of lethal metabolic crisis, i.e. extreme hypoglycemia. Several liver-intrinsic or -dependent processes may underlie the robust therapeutic effects we observed. The growth from the fetal period until the end of adolescence requires substantial amount of energy and metabolic resources. The growth of *Bcs1l*$^{p.S78G}$ mice rapidly slows down after 3 weeks of age, coinciding with a linear decrease in CIII activity[43]. Hepatocyte-targeted gene therapy partially restored hepatic *Igf-1*

and *Ghr* expression and improved growth, which indicates correction of growth signaling upon the restoration of hepatic mitochondrial metabolism. We previously showed that, despite the overall growth restriction, disproportionate MYC induction in the *Bcs1l*$^{p.S78G}$ mice drives cell proliferation and anabolism against lack of energy and biosynthetic resources, leading to hepatocyte senescence and contributing to the liver pathology[21]. rAAV-mediated restoration of CIII activity fully prevented the MYC induction and blunted cell proliferation, likely diverting resources from hepatocyte regeneration to systemic energy metabolism and growth.

The two most unexpected findings is this study were that the *Bcs1l*$^{p.S78G}$ mice apparently lack BAT activation and that hepatocyte-specific correction of CIII function normalized their body temperature. The total daily energy expenditure includes basal metabolism, the thermic effect of food, thermoregulation and physical activity. Basal metabolism, or the resting metabolic rate measured in the fed state at thermoneutrality, accounts for >50% of the total energy expenditure in mice[44]. In juvenile *Bcs1l*$^{p.S78G}$ mice, CIII activity is broadly decreased, by 50-90%, including in the liver and skeletal muscle, the largest heat-producing organs. Correspondingly, the weight-normalized night-time energy expenditure is 25-50% lower than that of wild-type littermates[22]. The mice are also small, which increases relative heat loss via skin, and they lack dermal adipose tissue. These aspects undoubtedly result in a great strain on the adaptive thermoregulatory system. Skeletal muscle is the largest heat-producing organ via both shivering and non-shivering thermogenesis (NST). The latter operates through sarcolipin-mediated uncoupling of the SERCA Ca^{2+} pump, and it can compensate for the loss of BAT thermogenesis in mice[40,45]. In the *Bcs1l*$^{p.S78G}$ skeletal muscle, upregulation of sarcolipin and related metabolism suggested an attempt, although insufficient, to maintain body temperature. Restoration of hepatic OXPHOS brought these markers back to wild-type level, suggesting that skeletal muscle NST is secondary to obligate (basal) NST in these mice, and demostrating stong metabolic crosstalk between these tissues.

The BAT is the major site for heat production in newborn humans and in small homeothermic animals like mice[46]. In a healthy animal, thermoreceptors in the skin and visceral organs detect cold exposure and transmit the signal to the hypothalamus. The hypothalamus stimulates sympathetic nerve termini in the BAT to release norepinephrine to activate the G protein-coupled ADRB3 receptor on brown adipocytes. ADRB3 stimulation leads to upregulation of mitochondrial biogenesis and UCP1 to increase mitochondrial mass and thermogenesis via OXPHOS uncoupling[36,46]. Surprisingly, both UCP1 expression and mitochondrial mass were unchanged in the hypothermic mutant mice, suggesting lack of thermogenic activation. A

possible explanation to this was that *Adrb3* expression was decreased to 10% of WT BAT even though BAT innervation as such was not decreased on the basis of TH quantification. Hot plate assay data from young adult (P100) *Bcs1l*$^{p.S78G}$ mice of the longer-living genetic background pointed to defective nociception, potentially affecting their ability to perceive and react appropriately to skin temperature. Consistent with this physiological data, neuronal marker stainings of hind limb foot pads showed severely disrupted or absent sensory neurons in the epidermis. The reduced hearing sensitivity in the same panel of adult *Bcs1l*$^{p.S78G}$ mice was consistent with peripheral neuropathy and with the sensorineural hearing loss typical in patients with *BCS1L* mutations[47–49]. Peripheral neuropathies are relatively common in mitochondrial diseases[50], but have not been reported in any mouse model of CIII deficiency. Given that the hypothalamus is the major neuronal regulator of energy expenditure including adaptive thermogenesis, through both hormonal and neuronal mechanisms[46], it is important to emphasize that the *Bcs1l*$^{p.S78G}$ mice do not develop the severe encephalopathy typical of many OXPHOS diseases. However, curiously, they do have local astrogliosis in the barrel field of the somatosensory cortex, which receives input from the whiskers[20,27], an important sensory organ in rodents.

Studies indicating the liver as a major thermogenic organ were published decades ago[51,52], but there is very scarce newer literature on the topic[53], perhaps because the field has since the 1970s focused on BAT thermogenesis, particularly in the context of obesity[54]. UCP1 is not expressed in the liver, precluding heat generation by mitochondrial uncoupling. Thus, the heat must originate from basal mitochondrial and non-mitochondrial metabolism. Strikingly, AAT-*Bcs1l* prevented the starvation-like hepatic glycogen depletion and fat accumulation in the *Bcs1l*$^{p.S78G}$ mice despite the continued low CIII activity and thus low OXPHOS in many other tissues. Gene expression data suggested a switch from glycolysis to fatty acid oxidation, but paradoxical downregulation of fatty acid oxidation in the CIII-deficient liver. This may be due to compromised β-oxidation, which feeds electrons to the coenzyme Q pool via electron-transferring flavoprotein dehydrogenase and is thus dependent on coenzyme Q oxidation by CIII[16]. The transcriptional response was fully normalized by the gene therapy, alleviating the energy metabolic stress locally in the liver and systemically. Interestingly, in the older (P150-200) mutants in the longer-living genetic background, *Hadhb* and *Cpt1a* are eventually upregulated and the livers lack fat accumulation[29,55], showing adjustment of the energy metabolism to the chronic CIII deficiency. Even though measuring the temperature of the liver *in vivo* is difficult, the most straightforward interpretation of our temperature, hepatic gene

expression and histologial data is that basal liver energy metabolism was normalized, resulting in restoration of basal heat production in mitochondria and by other basal metabolism. The liver being a large organ with very high blood flow, this was likely sufficient to maintain euthermia systemically.

The phenotype of the *Bcs1l*$^{p.S78G}$ mice shows some parallels with processes that cause so called BAT whitening. It has been descibed in rodent models of obesity, in thermoneutral housing, leptin receptor deficiency and chronic loss of adrenergic signaling[56]. Of these putative causes of whitening, the *Bcs1l*$^{p.S78G}$ mice clearly show loss of adrenergic signaling due to, as we suggest, sensory neuropathy. The absence of thermosensation in mice may induce a state of pseudo-thermoneutrality, potentially leading to similar effects on brown adipose tissue (BAT). The mice also have extremely low plasma leptin and thus lack of leptin receptor stimulation. Our findings emphasise the intricate interplay between mitochodria, hepatic energy metabolism, adaptive thermogenesis and thermosensation in thermoregulation, and reinforce the critical role of the liver as a thermogenic organ. Finally, our study highlightings the complexity of mitochondrial disease pathophysiology and the potential of tissue-targeted gene therapy to produce robust therapeutic effects despite, or sometimes because of, the complexity.

Materials and Methods

Cloning and virus production

Mouse *Bcs1l* coding sequence (*MmBcs1l*) was PCR-amplified from mouse tissue cDNA (primers EcoRI-MmBcs1l: 5'-ATGAATTCACCATGCCATTTTCAGACTTTGTTCTG-3' and MmBcs1l-STP-HindIII: 5'-ATAAGCTTTCACCTCAGAGATTCAATGTTGT-3'). The fragment was ligated into pBluescript and sequenced. The insert was subcloned into pAAV2-LSP1-PB(TR)-EGFP vector, which drives hepatocyte-specific expression under the human ApoE enhancer and α1-antitrypsin (AAT) promoter (generously provided by professor Ian Alexander, University of Sydney, Australia). The original vector containing Enhanced Green Fluorescent Protein (EGFP) cDNA was used as a control. Along with the expression cassette, the vectors also contained flanking PiggyBac transposon recognition sequences, which allow genomic integration upon parallel expression of PiggyBac transposase[26]. Serotype 9 viral particles were produced by the AAV Gene Transfer and Cell Therapy Core Facility of the University of Helsinki.

Mouse breeding and husbandry

The animal facilities of the University of Helsinki maintained the mice on the C57BL/6JCrl background (Harlan stock 000016). An *Bcs1l*$^{p.S78G}$ mutant strain carrying a spontaneous *mt-Cyb*$^{p.D254N}$ variant[22] was used throughout this study, with the exception of the thermoneutrality intervention and hot plate response measurement (see section below). In this mtDNA background, the homozygotes become terminally ill approximately 1 month of age, allowing fast assessment of survival. *Bcs1l* wildtype or heterozygous animals were used as healthy controls (wild type, WT, by phenotype) controls. Both males and females were used and data is shown separately for them only if a significant sex differences were observed or known.

The mice were housed in individually-ventilated cages with a 12-hour light/12-hour dark cycle at a temperature of 22-23°C, and they had ad libitum access to water and food (2018 Teklad global 18% protein rodent diet, Envigo). The animal studies were approved by the animal ethics committee of the State Provincial Office of Southern Finland (ESAVI/16278/2020 and ESAVI/31141/2023) and were performed according to FELASA (Federation of Laboratory Animal Science Associations) guidelines.

rAAV administration

Presymtomatic (postnatal day 19-23, P19-23) mutant mice were injected intraperitoneally with 100 µl saline containing 5×10^{10} viral particles encoding EGFP or wild-type BCS1L. Following the administration, the health of the mice was monitored visually and by weighing according to the ethical permit. Samples were collected at postnatal day 28 (P28) or according to the survival of the mice. In survival analysis, the mice were euthanized when weight loss was greater than 15% of the maximum weight of the individual mouse.

Thermoneutrality intervention, assessment of nociception and auditory brain stem response (ABR)

A group of *Bcs1l*$^{p.S78G}$ in a WT mtDNA backgroud were housed at 30-32°C for 10 days and sacrificed at P33. Hotplate test (thermal pain response) and hearing sensitivity assessment were carried out at the German Mouse Clinic, Munich, Germany on the same animal strain.

Assessment of body composition and temperature

Echo-MRI based MiniSpec Body Composition Analyzer (Bruker, Billerica, MA) was used to quantify fat mass. For measuring skin temperature, Gentle Temp 720 IR meter (Omron Health

Care) was used. The body temperature was estimated based on the skin temperature of sternum with the following formula: $Tbody = 163.9 + 11.47 * Tskin - 0.1629 * Tskin^2$. This formula derives from in-house calibration data from 33 mice from which both skin temperature and core temperature were measured. For the thermoneutrality experiment (explained above) the core temperature was measured by directly inserting the thermometer in the abdominal cavity.

Necropsy

The mice were euthanized either by cervical dislocation, or by administering a lethal dose of pentobarbital for blood collection through cardiac puncture. Before sample collection, the mice underwent a 2-hour fasting period, and all samples were obtained at similar time of the day, during the light period. Skin temperature was measured and spontaneously released urine samples collected before euthanasia. Tissues were either placed in 10% histology-grade formalin or frozen in liquid nitrogen and stored at -80°C. Blood glucose was measured with a stick meter (Freestyle lite, Abbott) from the blood within the body cavity while collecting the other samples.

Quantitative PCR (qPCR)

Total RNA was extracted from the snap-frozen tissue samples with RNAzol RT reagent (Sigma-Aldrich). cDNA was prepared using the strand cDNA Synthesis kit (Thermo Scientific) and qPCR performed using EvaGreen- and Phire II Hot Start DNA polymerase-based detection chemistry[22]. CFX96 thermocycler and CFX Manager software (Bio-Rad) were utilized to perform the qPCR and data analysis. LinRegPCR software[57] was used to calculate the PCR efficiency. List of all primers used can be found in Supplementary Table 1. *Gak* and *Rab11a* served as reference genes.

SDS-PAGE , blue-native PAGE and Western blot

For the analysis of albumin, urine samples were heated and mixed with Laemmli sample buffer, and an equivalent of 1µl of urine was loaded onto 4–20% tris-glycine polyacrylamide gel electrophoresis (PAGE) gels (Bio-Rad). The gels were stained with Coomassie G-250 and images were captured using a flatbed scanner.

For Western blot analyses of tissue samples, 5-10 mg frozen tissue samples were homogenized in SDS lysis buffer (2% SDS, 60 mM Tris-Cl pH 6.8, 12.5% glycerol, 1 mM EDTA) supplemented with protease inhibitors (Complete protease inhibitor mix, Roche). Sample

viscosity was reduced by sonication. To determine protein concentrations, Bradford reagent (Bio-Rad) was employed, and bovine serum albumin standards were used as reference. To mitigate interference from SDS, 2.5 mg/ml of α-cyclodextrin (Sigma-Aldrich) was added to the reagent[58]. For regular SDS-PAGE, bromphenol blue and 5% β-mercaptoethanol were added to the protein lysates. The samples were heated at 95ºC for 5 minutes, and 5–30 µg total protein per lane run in commercial gradient gels (Bio-Rad). Transfer to polyvinylidene fluoride (PVDF) (Amersham Hybond P 0.2 PVDF, Cytiva) membrane was achieved through the tank transfer method using standard Towbin transfer buffer containing 10% MeOH. To verify equal loading and transfer, the membranes were stained with Coomassie G-250. A list of all antibodies used can be found in Supplementary Table 2. Peroxidase-conjugated secondary antibodies, enhanced chemiluminescence, and the Bio-Rad ChemiDoc MP Imaging System with Image Lab software (Bio-Rad) were used for the detection and documentation of immunoreactions. All the samples were randomized before running and processing for quantification. For representative blots, individual samples were pooled from each experimental group to obtain an average signal, which represents each group.

For blue native gel electrophoresis (BNGE), liver mitochondria were first freshly isolated using the previously described protocol[22]. Then they were solubilized by adding 6 mg digitonin per mg of protein in cold buffer comprising (50 mM Bis-Tris-Cl^+, 50 mM NaCl, 1.4mg/ml digitonin, 10% glycerol, 1 mM EDTA, protease inhibitor mix, pH of 7.0). The sample lysates were clarified by centrifugation at 18,000g at +4°C for 6 minutes. Coomassie Blue G-250 (1.5 mg/ml) was added to the supernatants and 10 µg solubilized mitochondrial protein separated using 3–12% NativePAGE™ Bis-Tris gradient gels (Invitrogen) and electroransferred onto PVDF filters as described[22].

Assessment of respiratory chain enzymatic activities and quantification of ATP

CIII activity was measured from isolated mitochondria using a spectrophotometric method based on 550nm absorbance change upon cytochrome c reduction with decylubiquinol serving as the electron donor[22]. The background was determined in the presence of antimycin A and myxothiazol. The data were normalized to protein content.

Enzymatic quantification of ATP from liver was performed using previously described protocol[59].

Tissue histology, immunohistochemistry, and immunofluorescence

Formalin-fixed paraffin-embedded tissues underwent standard procedures for general histological assesment, including hematoxylin and eosin (H&E) staining (Sigma-Aldrich) and glycogen detection using periodic acid-Schiff (PAS) staining (Sigma-Aldrich). Additionally, frozen liver sections fixed in formalin and saturated with 30%$_{w/v}$ sucrose were subjected to the standard Oil-Red-O (ORO) staining (Sigma-Aldrich) to detect triglycerides. The antigen retrieval of paraffin sections for cleaved caspase 3 and HSP60 staining (see supplementary Table 2) was done by immersing the slides in 10 mM Tris-Cl, pH 9.0; 1mM EDTA, and boiled for 15 minutes. After incubating the sections in the primary antibody, ImmPress peroxidase- or alkaline phosphatase polymer-conjugated of secondary antibodies (Vector Laboratories Inc) were added. Nitroblue teterazolium was used to visualize alkaline phosphatase and diaminobenzidine peroxidase activity, respectively. Nuclear Fast Red (Sigma-Aldrich) and hematoxylin were used as nuclear counterstains for alkaline phosphatase and peroxidase stainings, respectively. Image acquisition was performed with Zeiss Axio Imager M2 microscope, Axiocam 503 camera, and Zen 2.3 software (Zeiss).

Sensory neurons were detected by immunofluorescence staining of the hind limb paw foot pads (see supplementary Table 2), followed by counterstaining with Hoechst nuclear stain. Image acquisition was then performed by the Andor Dragonfly spinning disc microscope with Zyla 4.2 sCMOS camera (Andor technology).

Statistics

All the samples were randomized before running and processing for quantification. For data that followed normal distribution, we applied a one-way ANOVA, followed by selected comparisons using t-tests with Welch's correction. Survival curves were analyzed using the log-rank Mantel–Cox test. We conducted these statistical analyses using GraphPad Prism 10 software (GraphPad Software Inc.).

Acknowledgements

We thank Vilma Wanne for technical assistance, professor Ian Alexander for (University of Sydney) for providing the pAAV-LSP1 plasmids and Christa Kietz for critical reading of the manuscript. We thank German mouse clinic (Munich) for mouse phenotyping report. We also thank the core facilities of University of Helsinki, FIMM Digital Microscopy and Molecular

Pathology Unit, and the Finnish Centre for Laboratory Animal Pathology (Faculty of Veterinary Medicine) for processing of histological samples, Biomedicum Imaging Unit for microscopy services and the Laboratory Animal Center of the University of Helsinki for the animal husbandry. We acknowledge the funding from Folkhälsan Research Center, Jane and Aatos Erkko Foundation, the Foundation for Pediatric Research, Finska Läkaresällskapet, The Liv och Hälsa Foundation, Magnus Ehrnrooth Foundation, the Finnish Society of Sciences and Letters and Finnish Doctoral Programme in Oral Sciences (FINDOS). Graphical illustrations in Fig. 1A, B and 7 were created with BioRender (https://www.biorender.com/).

Author contributions

R.B., J.P., V.F., S.K. and J.K. designed the study. R.B. wrote the first manuscript draft and prepared the figure panels. R.B., J.P., and J.K performed the animal experiments and sample collection. R.B, J.P. and J.K. performed the histological analyses. The contributions for other methods were following: body composition analyses (R.B. and J.P.), SDS-PAGE and Western blot analyses (R.B., D.U. and J.K.), Blue-Native PAGE (R.B. and J.P.), qPCR (R.B.), immunohistochemistry (J.K.), ATP measurements (R.B. and J.P) and immunofluorescence staining (T.Z.). R.B. was responsible for the statistics. All authors critically read and commented the manuscript, and R.B. and J.K. revised it accordingly.

References

1. Suomalainen, A., and Nunnari, J. (2024). Mitochondria at the crossroads of health and disease. Cell 187, 2601–2627.

2. Castillo-Armengol, J., Fajas, L., and Lopez-Mejia, I.C. (2019). Inter-organ communication: a gatekeeper for metabolic health. EMBO Rep. 20, e47903.

3. Boardman, N.T., Trani, G., Scalabrin, M., Romanello, V., and Wüst, R.C.I. (2023). Intracellular to interorgan mitochondrial communication in striated muscle in Health and disease. Endocr. Rev. 44, 668–692.

4. Russell, O.M., Gorman, G.S., Lightowlers, R.N., and Turnbull, D.M. (2020). Mitochondrial diseases: hope for the future. Cell 181, 168–188.

5. Soldatov, V.O., Kubekina, M.V., Skorkina, M.Yu., Belykh, A.E., Egorova, T.V., Korokin, M.V., Pokrovskiy, M.V., Deykin, A.V., and Angelova, P.R. (2022). Current advances in gene therapy of mitochondrial diseases. J. Transl. Med. 20, 562.

6. Sarzi, E., Seveno, M., Piro-Mégy, C., Elzière, L., Quilès, M., Péquignot, M., Müller, A., Hamel, C.P., Lenaers, G., and Delettre, C. (2018). OPA1 gene therapy prevents retinal ganglion cell loss in a Dominant optic atrophy mouse model. Sci. Rep. 8, 2468.

7. Suzuki-Hatano, S., Saha, M., Soustek, M.S., Kang, P.B., Byrne, B.J., Cade, W.T., and Pacak, C.A. (2019). *AAV9-TAZ* gene replacement ameliorates cardiac TMT proteomic profiles in a mouse model of Barth syndrome. Mol. ther., Methods clin. dev. 13, 167–179.

8. Perdomini, M., Belbellaa, B., Monassier, L., Reutenauer, L., Messaddeq, N., Cartier, N., Crystal, R.G., Aubourg, P., and Puccio, H. (2014). Prevention and reversal of severe mitochondrial cardiomyopathy by gene therapy in a mouse model of Friedreich's ataxia. Nat. Med. 20, 542–547.

9. Bottani, E., Giordano, C., Civiletto, G., Di Meo, I., Auricchio, A., Ciusani, E., Marchet, S., Lamperti, C., d'Amati, G., Viscomi, C., et al. (2014). AAV-mediated liver-specific MPV17 expression restores mtdna levels and prevents diet-induced liver failure. Mol. Ther. 22, 10–17.

10. Torres-Torronteras, J., Cabrera-Pérez, R., Vila-Julià, F., Viscomi, C., Cámara, Y., Hirano, M., Zeviani, M., and Martí, R. (2018). Long-term sustained effect of liver-targeted adeno-associated virus gene therapy for mitochondrial neurogastrointestinal encephalomyopathy. Hum. Gene Ther. 29, 708–718.

11. Silva-Pinheiro, P., Cerutti, R., Luna-Sanchez, M., Zeviani, M., and Viscomi, C. (2020). A single intravenous injection of AAV-PHP.B-*hNDUFS4* ameliorates the phenotype of *Ndufs4−/−* mice. Mol. ther., Methods clin. dev. 17, 1071–1078.

12. Reynaud-Dulaurier, R., Benegiamo, G., Marrocco, E., Al-Tannir, R., Surace, E.M., Auwerx, J., and Decressac, M. (2020). Gene replacement therapy provides benefit in an adult mouse model of Leigh syndrome. Brain 143, 1686–1696.

13. Di Meo, I., Auricchio, A., Lamperti, C., Burlina, A., Viscomi, C., and Zeviani, M. (2012). Effective AAV-mediated gene therapy in a mouse model of Ethylmalonic encephalopathy. EMBO Mol. Med. 4, 1008–1014.

14. Lopez-Gomez, C., Sanchez-Quintero, M.J., Lee, E.J., Kleiner, G., Tadesse, S., Xie, J., Akman, H.O., Gao, G., and Hirano, M. (2021). Synergistic deoxynucleoside and gene therapies for thymidine kinase 2 deficiency. Ann. Neurol. 90, 640–652.

15. Slone, J., and Huang, T. (2020). The special considerations of gene therapy for mitochondrial diseases. NPJ Genom. Med. 5, 1–7.

16. Banerjee, R., Purhonen, J., and Kallijärvi, J. (2022). The mitochondrial coenzyme Q junction and complex III: biochemistry and pathophysiology. FEBS J. 289, 6936–6958.

17. Fellman, V., Rapola, J., Pihko, H., Varilo, T., and Raivio, K.O. (1998). Iron-overload disease in infants involving fetal growth retardation, lactic acidosis, liver haemosiderosis, and aminoaciduria. Lancet 351, 490–493.

18. Visapää, I., Fellman, V., Vesa, J., Dasvarma, A., Hutton, J.L., Kumar, V., Payne, G.S., Makarow, M., Van Coster, R., Taylor, R.W., et al. (2002). GRACILE Syndrome, a lethal metabolic disorder with iron overload, is caused by a point mutation in BCS1L. Am. J. Hum. Genet. 71, 863–876.

19. Levéen, P., Kotarsky, H., Mörgelin, M., Karikoski, R., Elmér, E., and Fellman, V. (2011). The GRACILE mutation introduced into *Bcs1l* causes postnatal complex III deficiency: A viable mouse model for mitochondrial hepatopathy. Hepatology 53, 437–447.

20. Rajendran, J., Purhonen, J., Tegelberg, S., Smolander, O.-P., Mörgelin, M., Rozman, J., Gailus-Durner, V., Fuchs, H., Hrabe de Angelis, M., Auvinen, P., et al. (2019). Alternative oxidase-mediated respiration prevents lethal mitochondrial cardiomyopathy. EMBO Mol. Med. 11.

21. Purhonen, J., Banerjee, R., Wanne, V., Sipari, N., Mörgelin, M., Fellman, V., and Kallijärvi, J. (2023). Mitochondrial complex III deficiency drives c-MYC overexpression and illicit cell cycle entry leading to senescence and segmental progeria. Nat. Commun. 14, 2356. 38027-1.

22. Purhonen, J., Grigorjev, V., Ekiert, R., Aho, N., Rajendran, J., Pietras, R., Truvé, K., Wikström, M., Sharma, V., Osyczka, A., et al. (2020). A spontaneous mitonuclear epistasis converging on Rieske Fe-S protein exacerbates complex III deficiency in mice. Nat. Commun. 11, 322.

23. Tomašić, N., Kotarsky, H., de Oliveira Figueiredo, R., Hansson, E., Mörgelin, M., Tomašić, I., Kallijärvi, J., Elmér, E., Jauhiainen, M., Eklund, E.A., et al. (2020). Fasting reveals largely intact systemic lipid mobilization mechanisms in respiratory chain complex III deficient mice. Biochim. Biophys. Acta, Mol. Basis Dis. 1866, 165573.

24. Baruteau, J., Brunetti-Pierri, N., and Gissen, P. (2024). Liver-directed gene therapy for inherited metabolic diseases. JIMD 47, 9–21.

25. Logan, G.J., de Alencastro, G., Alexander, I.E., and Yeoh, G.C. (2014). Exploiting the unique regenerative capacity of the liver to underpin cell and gene therapy strategies for genetic and acquired liver disease. Int. J. Biochem. Cell Biol. 56, 141–152.

26. Cunningham, S.C., Siew, S.M., Hallwirth, C.V., Bolitho, C., Sasaki, N., Garg, G., Michael, I.P., Hetherington, N.A., Carpenter, K., de Alencastro, G., et al. (2015). Modeling correction of severe urea cycle defects in the growing murine liver using a hybrid recombinant adeno-associated virus/piggyBac transposase gene delivery system. Hepatology 62, 417–428.

27. Tegelberg, S., Tomašić, N., Kallijärvi, J., Purhonen, J., Elmér, E., Lindberg, E., Nord, D.G., Soller, M., Lesko, N., Wedell, A., et al. (2017). Respiratory chain complex III deficiency due to mutated BCS1L: a novel phenotype with encephalomyopathy, partially phenocopied in a *Bcs1l* mutant mouse model. Orphanet J. Rare Dis. 12, 73.

28. Rajendran, J., Tomašić, N., Kotarsky, H., Hansson, E., Velagapudi, V., Kallijärvi, J., and Fellman, V. (2016). Effect of high-carbohydrate diet on plasma metabolome in mice with mitochondrial respiratory chain complex iii deficiency. Int. J. Mol. Sci. 17.

29. Purhonen, J., Rajendran, J., Tegelberg, S., Smolander, O.-P., Pirinen, E., Kallijärvi, J., and Fellman, V. (2018). NAD+ repletion produces no therapeutic effect in mice with respiratory chain complex III deficiency and chronic energy deprivation. FASEB J., fj201800090R.

30. Purhonen, J., Rajendran, J., Mörgelin, M., Uusi-Rauva, K., Katayama, S., Krjutskov, K., Einarsdottir, E., Velagapudi, V., Kere, J., Jauhiainen, M., et al. (2017). Ketogenic diet attenuates hepatopathy in mouse model of respiratory chain complex III deficiency caused by a Bcs1l mutation. Sci. Rep. 7.

31. Molitoris, B.A., Sandoval, R.M., Yadav, S.P.S., and Wagner, M.C. (2022). Albumin uptake and processing by the proximal tubule: physiological, pathological, and therapeutic implications. Physiol. Rev. 102, 1625–1667.

32. Dittner, C., Lindsund, E., Cannon, B., and Nedergaard, J. (2019). At thermoneutrality, acute thyroxine-induced thermogenesis and pyrexia are independent of UCP1. Mol. Metab. 25, 20–34.

33. Sentis, S.C., Oelkrug, R., and Mittag, J. (2021). Thyroid hormones in the regulation of brown adipose tissue thermogenesis. Endocr. Connect. 10, R106–R115.

34. Friedman, J.M. (2019). Leptin and the endocrine control of energy balance. Nat. Metab. 1, 754–764.

35. Fischer, A.W., Cannon, B., and Nedergaard, J. (2020). Leptin: Is It thermogenic? Endocr. Rev. 41, 232–260.

36. Xue, S., Lee, D., and Berry, D.C. (2023). Thermogenic adipose tissue in energy regulation and metabolic health. Front. Endocrinol. (Lausanne) 14, 1150059.

37. Auger, C., and Kajimura, S. (2023). Adipose tissue remodeling in pathophysiology. Annu. Rev. Pathol. 18, 71–93. https://doi.org/10.1146/annurev-pathol-042220-023633.

38. Valentine, J.M., Ahmadian, M., Keinan, O., Abu-Odeh, M., Zhao, P., Zhou, X., Keller, M.P., Gao, H., Yu, R.T., Liddle, C., et al. (2022). β3-Adrenergic receptor downregulation leads to adipocyte catecholamine resistance in obesity. J. Clin. Invest. 132.

39. Fedorenko, A., Lishko, P.V., and Kirichok, Y. (2012). Mechanism of fatty-acid-dependent UCP1 uncoupling in brown fat mitochondria. Cell 151, 400–413.

40. Bal, N.C., Maurya, S.K., Sopariwala, D.H., Sahoo, S.K., Gupta, S.C., Shaikh, S.A., Pant, M., Rowland, L.A., Bombardier, E., Goonasekera, S.A., et al. (2012). Sarcolipin is a newly identified regulator of muscle-based thermogenesis in mammals. Nat. Med. 18, 1575–1579.

41. Maurya, S.K., Herrera, J.L., Sahoo, S.K., Reis, F.C.G., Vega, R.B., Kelly, D.P., and Periasamy, M. (2018). Sarcolipin signaling promotes mitochondrial biogenesis and oxidative metabolism in skeletal muscle. Cell Rep. 24, 2919–2931.

42. Maurya, S.K., Bal, N.C., Sopariwala, D.H., Pant, M., Rowland, L.A., Shaikh, S.A., and Periasamy, M. (2015). Sarcolipin is a key determinant of the basal metabolic rate, and its overexpression enhances energy expenditure and resistance against diet-induced obesity. J. Biol. Chem. *290*, 10840–10849.

43. Levéen, P., Kotarsky, H., Mörgelin, M., Karikoski, R., Elmér, E., and Fellman, V. (2011). The GRACILE mutation introduced into *Bcs1l* causes postnatal complex III deficiency: A viable mouse model for mitochondrial hepatopathy. Hepatology 53, 437–447.

44. Brzęk, P., Gębczyński, A., Selewestruk, P., Książek, A., Sadowska, J., and Konarzewski, M. (2022). Significance of variation in basal metabolic rate in laboratory mice for translational experiments. J. Comp. Physiol. B 192, 161–169.

45. Bal, N.C., Maurya, S.K., Singh, S., Wehrens, X.H.T., and Periasamy, M. (2016). Increased reliance on muscle-based thermogenesis upon acute minimization of brown adipose tissue function. J. Biol. Chem 291, 17247–17257.

46. Tran, L.T., Park, S., Kim, S.K., Lee, J.S., Kim, K.W., and Kwon, O. (2022). Hypothalamic control of energy expenditure and thermogenesis. Exp. Mol. Med. 54, 358–369.

47. Hikmat, O., Isohanni, P., Keshavan, N., Ferla, M.P., Fassone, E., Abbott, M., Bellusci, M., Darin, N., Dimmock, D., Ghezzi, D., et al. (2021). Expanding the phenotypic spectrum of BCS1L-related mitochondrial disease. Ann. Clin. Transl. Neurol. 8, 2155–2165.

48. Hinson, J.T., Fantin, V.R., Schönberger, J., Breivik, N., Siem, G., McDonough, B., Sharma, P., Keogh, I., Godinho, R., Santos, F., et al. (2007). Missense mutations in the BCS1L gene as a cause of the Björnstad syndrome. N. Engl. J. Med.aj 356, 809–819.

49. Jackson, C.B., Bauer, M.F., Schaller, A., Kotzaeridou, U., Ferrarini, A., Hahn, D., Chehade, H., Barbey, F., Tran, C., Gallati, S., et al. (2016). A novel mutation in BCS1L associated with deafness, tubulopathy, growth retardation and microcephaly. Eur. J. Pediatr. 175, 517–525.

50. Horvath, R., Medina, J., Reilly, M.M., Shy, M.E., and Zuchner, S. (2023). Peripheral neuropathy in mitochondrial disease. Handb. Clin. Neurol. 194, 99–116.

51. Kawahata, A., and Carlson, L.D. (1959). Role of rat liver in nonshivering thermogenesis. Proc. Soc. Exp. Biol. Med.

52. Stoner, H.B. (1973). The role of the liver in non-shivering thermogenesis in the rat. J. Physiol. 232, 285–296.

53. Abumrad, N.A. (2017). The liver as a hub in thermogenesis. Cell Metab. 26, 454–455.

54. Trayhurn, P. (2017). Origins and early development of the concept that brown adipose tissue thermogenesis is linked to energy balance and obesity. Biochimie. 134, 62–70.

55. Purhonen, J., Rajendran, J., Mörgelin, M., Uusi-Rauva, K., Katayama, S., Krjutskov, K., Einarsdottir, E., Velagapudi, V., Kere, J., Jauhiainen, M., et al. (2017). Ketogenic diet attenuates hepatopathy in mouse model of respiratory chain complex III deficiency caused by a Bcs1l mutation. Sci. Rep. 7, 957.

56. Kotzbeck, P., Giordano, A., Mondini, E., Murano, I., Severi, I., Venema, W., Cecchini, M.P., Kershaw, E.E., Barbatelli, G., Haemmerle, G., et al. (2018). Brown adipose tissue whitening leads to brown adipocyte death and adipose tissue inflammation. J. Lipid Res. 59, 784–794.

55. Kotzbeck, P., Giordano, A., Mondini, E., Murano, I., Severi, I., Venema, W., Cecchini, M.P., Kershaw, E.E., Barbatelli, G., Haemmerle, G., et al. (2018). Brown adipose tissue whitening leads to brown adipocyte death and adipose tissue inflammation[S]. J. Lipid Res. 59, 784–794.

57. Gamal, M., and Ibrahim, M.A. (2024). Introducing the f0% method: a reliable and accurate approach for qPCR analysis. BMC Bioinformatics 25.

58. Rabilloud, T. (2018). Optimization of the cydex blue assay: A one-step colorimetric protein assay using cyclodextrins and compatible with detergents and reducers. PLOS ONE 13, e0195755.

59. Purhonen, J., Hofer, A., and Kallijärvi, J. (2023). Quantification of all 12 canonical ribonucleotides by real-time fluorogenic in vitro transcription. Nucleic Acids Res. 52, e6.

Figure legends

Figure 1. rAAV-based gene replacement therapy in CIII-deficient *Bcs1l*$^{p.S78G}$ mice

A) Schematic presentation of the experimental setup.
B) Schematic presentation of the experimental timeline and the time points of the investigations performed in this study.
C) Total and virally-expressed *Bcs1l* mRNA at P28 (*n*=7-8/group).
D) Survival curves of rAAV-*EGFP* and three different groups of rAAV-*Bcs1l* injected mutant mice are shown (*n*=5-8/group).
E) Total *Bcs1l* mRNA at the end stage of the survival study (*n*=4-16/group).
F) Blood glucose levels (in mmol/L) of all the groups (*n*=4-17/group). The dotted line represents the critical level of glucose (<2.5mmol/L).
G) Sex segregated growth rate of the mice from P25 to P28 (n=6-13/group).
H-I) Hepatic mRNA expression of insulin-like growth factor 1 (*Igf1*) and growth hormone receptor (*Ghr*) at P28 (*n*=7-8/group).

Statistics: Mann-Whitney U test (C & E). One-way ANOVA followed by the selected pairwise comparisons with Welch's t-statistics (F-I) and Survival data were analyzed with log-rank test (Mantel–Cox). A log transformation before Welch's t-statistics was performed in E. *p* values of the group comparisons are indicated above the panel. **p*, comparison between survival of AAT-*Bcs1l* and CAG-*Bcs1l* group. The error bars stand for standard deviation. All data points derive from independent mice.

Figure 2. Hepatic CIII assembly, activity, and mitochondrial mass in juvenile mice injected with rAAVs

A) Representative Blue-Native PAGE blot of RISP and CORE1 assembled into free $CIII_2$ and supercomplexes (SCs) in isolated mitochondria at P28, and RISP per CORE1 ratio in free $CIII_2$ (*n*=4/group).
B) CIII activity in isolated mitochondria at P28 (*n* = 4/group).
C) ATP in liver at P28 (*n* = 6-7/group).
D) mRNA expression of transcriptional regulators of mitochondrial biogenesis *Ppargc1a (PGC-1α)*, from P28 liver (*n*=7-8/group).
E) Western blot quantification and representative blot of the indicated markers for mitochondrial mass (HSP60 & VDAC1) from P28 liver lysates (*n*=6-8/group).

Statistics: Welch's *t*-test (A) and one-way ANOVA followed by the selected pairwise comparisons with Welch's t-statistics (B-E). P values of the group comparisons are indicated above the panel. The error bars stand for standard deviation. All data points derive from independent mice.

Figure 3. Effect of hepatocyte-targeted gene replacement on hepatopathy

A-D) Representative images of H&E-stained liver sections (*n*=6-7/group) showing tissue morphology and expansion of portal areas (shown by dotted lines), Oil Red O staining of liver cryosections (*n*=4/group) showing lipid accumulation, periodic acid-Schiff (PAS)

stained liver sections (*n*=5/group) detecting glycogen and immunostainings of liver sections for apoptotic cell marker, cleaved caspase 3 (cc3) (*n*=5/group) at P28.

E-F) Quantification of the hepatic ductular reactions and the apoptotic cells from H&E-stained and cc3- immunostained sections, respectively.

G-H) *Gsta1* and *Gdf15* mRNA from P28 liver (*n*=7-8/group)

Statistics: Mann-Whitney U test (E) one-way ANOVA followed by the selected pairwise comparisons with Welch's t-statistics (F-H). P values of the group comparisons are indicated above the panel. The error bars stand for standard deviation. All data points derive from independent mice.

Figure 4. Effect of hepatocyte-targeted gene replacement on hepatic cell proliferation and cellular senescence

A-D) Western blot quantification and representative blot of γH2AX, CDKN1A, c-Myc and PCNA and Cyclin A2 from P28 liver lysates (*n*=6-8/group).

E-F) *Ctsl* and *Gpnmb* mRNA from P28 liver (*n*=7-8/group).

Statistics: one-way ANOVA followed by the selected pairwise comparisons with Welch's t-statistics. P values of the group comparisons are indicated above the panel. The error bars stand for standard deviation. All data points derive from independent mice.

Figure 5. Body temperature and thermosensation in the *Bcs1l*$^{p.S78G}$ mice

A-B) Estimated core temperature of P28 mice (n=14-21/group).

C) Cold inducible gene expressions from P28 liver (n=7-8/group).

D) Estimated core temperature of *Bcs1l*$^{p.S78G}$ mice at P30 after housing them at thermoneutral temperature (30-32°C) for 10 days (*n*=4 -6/group).

E) Hot plate response time of *Bcs1l*$^{p.S78G}$ mice at P100 (n=19-20/group).

F) Representative image of WT and mutant foot pad neurons stained with TUJ1, CGRP and NF-M. The red arrows indicates the stained neurons (*n*=3-4/group).

Statistics: one-way ANOVA followed by the selected pairwise comparisons with Welch's t-statistics (B-D), Mann-Whitney U test (E) . The error bars stand for standard deviation. All data points derive from independent mice.

Figure 6. Effect of liver-targeted gene replacement on adaptive thermogenesis and energy metabolism

A) Western blot quantification and representative blot of tyrosine hydroxylase from P28 BAT lysates (*n*=6-8/group).

B) *Adrb3* mRNA from P28 BAT (n=6-8/group).

C) Western blot quantification and representative blot of UCP1 from P28 BAT lysates (*n*=6-8/group).

D-H) *Ucp1, Dio2, Cidea, Prdm16* and *Ppargc1a* mRNA from P28 BAT (n=6-8/group)

I) Western blot quantification and representative blot of HSP60 and SDHA from P28 BAT lysates (*n*=6-8/group).

J-N) *Sln, Ppargc1a,* gene expression of markers for mitochondrial mass (*Ndufs3* and *Sdhb*) *Pdk4,*

and *Cd36* mRNA from P28 quadriceps (n=6-8/group).

O-S) *Pdk4, Cd36, Pparα, Hadhb and Cpt1a* mRNA from P28 liver (*n*=7-8/group).

T) Western blot quantification and representative blot of the phosphorylation status of AMPKα from P28 liver lysates (*n*=6-8/group)

Statistics: one-way ANOVA followed by the selected pairwise comparisons with Welch's t-statistics (A-C, F-I, L & N-T). Mann-Whitney U test (D, E, J, K & M). The error bars stand for standard deviation. All data points derive from independent mice.

Figure 7. Schematic presentation of the proposed mechanism for maintaining euthermia in mutant mice with hepatocyte-specific restoration of OXPHOS

Supplementary figure 1. Transduction efficiency of the liver by rAAVs

A) Representative image for transduction effeciency of the liver-targeted viral vector.

B) Appearence of the liver at P28 after receiving liver targeted gene therapy.

C) Virally expressed *Bcs1l* mRNA at the end stage of the survival study (*n*=4-17/group).

D) Representative images of immunostainings of liver sections for mitochondrial marker, HSP60.

Statistics: Mann-Whitney U test (C & D). P values of the group comparisons are indicated above the panel. The error bars stand for standard deviation. All data points derive from independent mice.

Supplementary figure 2. End-stage liver in mutant mice after hepatocyte-targeted gene replacement therapy

A-C) Representative images of H&E-stained liver sections (*n*=5/group) showing tissue. morphology, periodic acid-Schiff (PAS) stained liver sections (*n*=5/group) detecting glycogen and immunostainings of liver sections for apoptotic cell marker, cleaved caspase 3 (cc3) (*n*=5/group) at the end stage of survival study.

D-E) Quantification of the hepatic ductular reactions and the apoptotic cells from H&E-statined sections and cc3 immunostained sections, respectively.

F-I) *Gsta1,Gdf15, Cstl* and *Gpnmb* mRNA from liver of the survival cohort (*n*=4/group).

Statistics: Welch's *t*-test. The error bars stand for standard deviation. P values of the group comparisons are indicated above the panel. All data points derive from independent mice.

Supplementary figure 3. Effect of hepatocyte-targeted gene replacement on kidney manifestations

A-B) Representative images of H&E-stained kidney sections (n=6-7/group) showing tissue morphology and immunostainings of cleaved caspase 3 (cc3) (n=5/group) showing apoptotic cells in kidney from P28 mice.

C-D) Quantification of kidney cortex thickness and the apoptotic cells, from H&E-stained and cc3-immunostatined sections, respectively from P28 mice.

E-F) Representative images of H&E-stained kidney sections (n=4/group) showing tissue morphology and immunostainings of cleaved caspase 3 (cc3) (n=5/group) showing apoptotic

cells in kidney from survival AAT-*Bcs1l* +PiggyBac and CAG-*Bcs1l* panel.

G-H) Quantification of kidney cortex thickness and the apoptotic cells, from H&E-stained and cc3-immunostatined sections (*n*=5/group), respectively from survival AAT-*Bcs1l* +PiggyBac panel.

I-J) Quantification of kidney cortex thickness and the apoptotic cells, from H&E-stained and cc3-immunostatined sections (*n*=5/group), respectively from survival CAG-*Bcs1l* panel.

K-L) Representative image of SDS-PAGE analysis of male mouse urine for albuminuria from P28 and survival AAT-*Bcs1l* panel and its quantification.

Statistics: one-way ANOVA followed by the selected pairwise comparisons with Welch's t-statistics (C, D & L) and Welch's *t*-test (G-J). P values of the group comparisons are indicated above the panel. The error bars stand for standard deviation. All data points derive from independent mice.

Supplementary figure 4. End-stage body temperature and adaptive thermogenesis in *Bcs1l*$^{p.S78G}$ mice

A) Body temperature of the end stage survival cohort (*n*=5/group).

B) Cold inducible gene expressions of the end stage survival cohort (*n*=4/group).

C) Auditory brain stem response of *Bcs1l*$^{p.S78G}$ mice (n=19-20/group).

D) Plasma thyroid hormone levels of P28 panel (n=4-10/group).

E) Skin temperature of EGFP and T3 injected P28 mutant mice (n=3-5/group).

F) Dual-energy X-ray absorptiometry (DEXA) analysis (*n* = 3-6/group) of fat mass, and at P28 and survival mice.

G) Plasma leptin levels of P115 *Bcs1l*$^{p.S78G}$ mice (n=8/group).

H) Representative image of WT and mutant foot pad neurons stained with NF-H (*n*=3-4/group).

Statistics: Welch's *t*-test (A, B & D). Mann-Whitney U test (B & E) one-way ANOVA followed by the selected pairwise comparisons with Welch's t-statistics (C & F). P values of the group comparisons are indicated above the panel. The error bars stand for standard deviation. All data points derive from independent mice.

Supplementary figure 5. Effect of hepatocyte-targeted gene replacement on adaptive thermogenesis and energy metabolism

A) *Trib1* mRNA from P28 BAT (n=6-8/group).

B) Representative blot of the phosphorylation status of AMPKα from P28 liver lysates (*n*=6-8/group)

C-E) *Pdk4, Cd36 and Pparα* mRNA from liver of the end stage survival cohort (*n*=4/group).

Statistics: one-way ANOVA followed by the selected pairwise comparisons with Welch's t-statistics (A & B) and Welch's *t*-test (C-E). P values of the group comparisons are indicated above the panel. The error bars stand for standard deviation. All data points derive from independent mice.

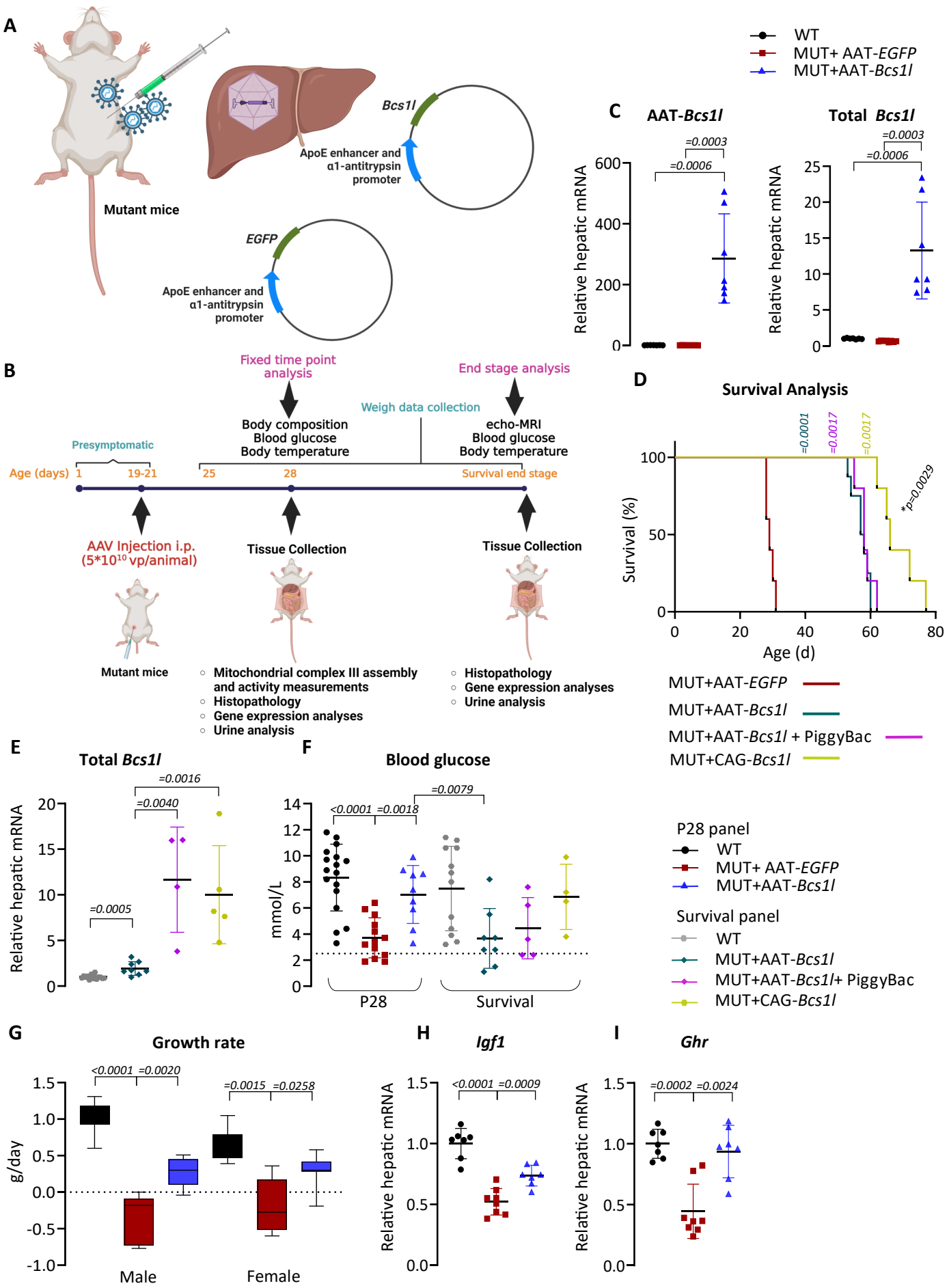
A
Mutant mice
Bcs1l
ApoE enhancer and α1-antitrypsin promoter
EGFP
ApoE enhancer and α1-antitrypsin promoter
WT
MUT+ AAT-EGFP
MUT+AAT-Bcs1l
C
AAT-Bcs1l
Total Bcs1l
Relative hepatic mRNA
=0.0003
=0.0006
B
Fixed time point analysis
End stage analysis
Weigh data collection
Body composition
Blood glucose
Body temperature
echo-MRI
Blood glucose
Body temperature
Presymptomatic
Age (days) 1 19-21 25 28 Survival end stage
AAV Injection i.p. (5*10^10 vp/animal)
Tissue Collection
Tissue Collection
Mutant mice
Mitochondrial complex III assembly and activity measurements
Histopathology
Gene expression analyses
Urine analysis
Histopathology
Gene expression analyses
Urine analysis
D
Survival Analysis
Survival (%)
Age (d)
=0.0001
=0.0017
=0.0017
*p=0.0029
MUT+AAT-EGFP
MUT+AAT-Bcs1l
MUT+AAT-Bcs1l + PiggyBac
MUT+CAG-Bcs1l
E
Total Bcs1l
Relative hepatic mRNA
=0.0005
=0.0040
=0.0016
F
Blood glucose
mmol/L
<0.0001
=0.0018
=0.0079
P28
Survival
P28 panel
WT
MUT+ AAT-EGFP
MUT+AAT-Bcs1l
Survival panel
WT
MUT+AAT-Bcs1l
MUT+AAT-Bcs1l+ PiggyBac
MUT+CAG-Bcs1l
G
Growth rate
g/day
<0.0001
=0.0020
=0.0015
=0.0258
Male
Female
H
Igf1
Relative hepatic mRNA
<0.0001
=0.0009
I
Ghr
Relative hepatic mRNA
=0.0002
=0.0024

Fig:1

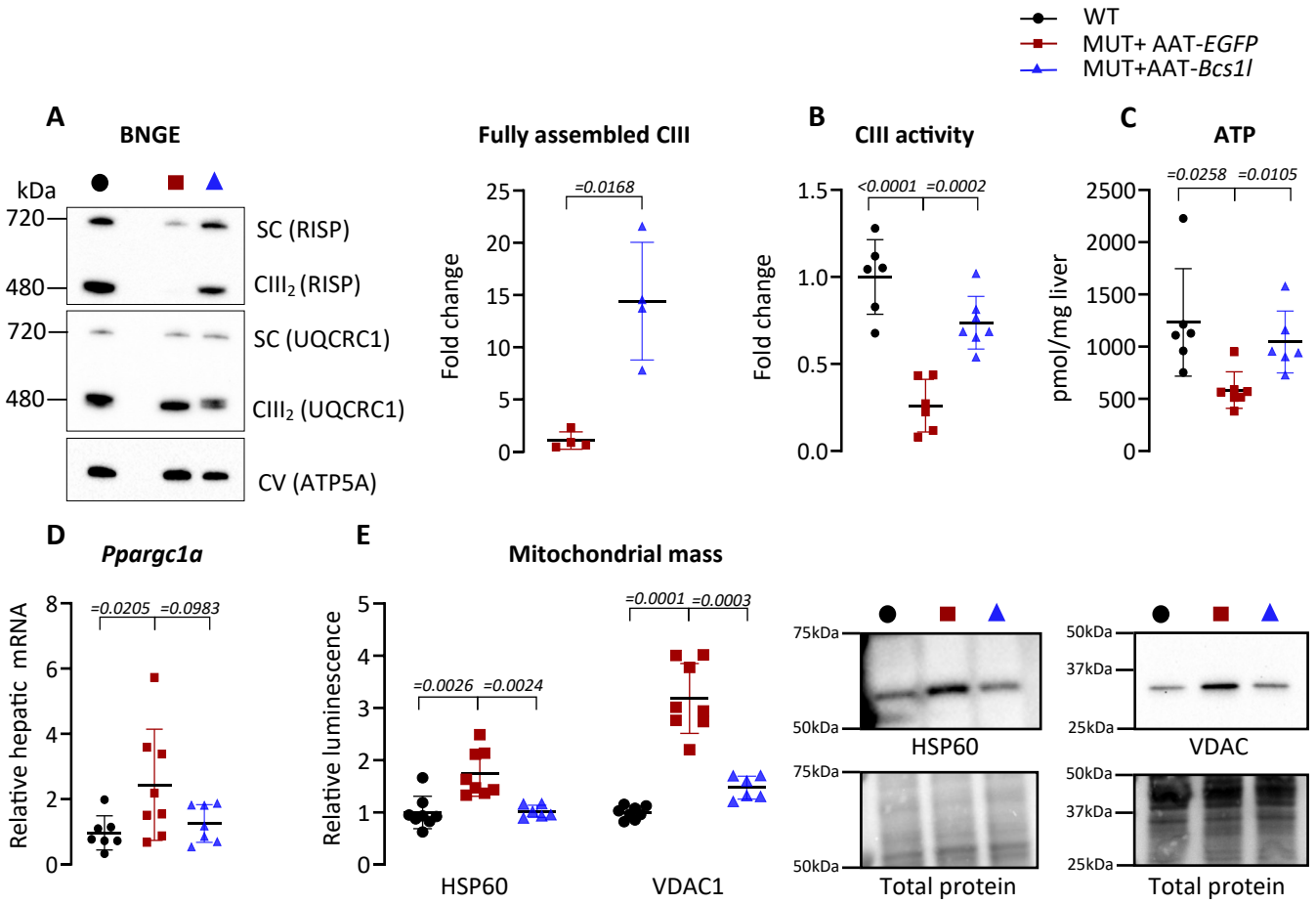
WT
MUT+ AAT-EGFP
MUT+AAT-Bcs1l
A
BNGE
kDa
720
480
720
480
SC (RISP)
CIII2 (RISP)
SC (UQCRC1)
CIII2 (UQCRC1)
CV (ATP5A)
Fully assembled CIII
Fold change
=0.0168
B
CIII activity
Fold change
<0.0001
=0.0002
C
ATP
pmol/mg liver
=0.0258
=0.0105
D
Ppargc1a
Relative hepatic mRNA
=0.0205
=0.0983
E
Mitochondrial mass
Relative luminescence
=0.0026
=0.0024
=0.0001
=0.0003
HSP60
VDAC1
75kDa
50kDa
HSP60
Total protein
50kDa
37kDa
25kDa
VDAC
Total protein

Fig:2

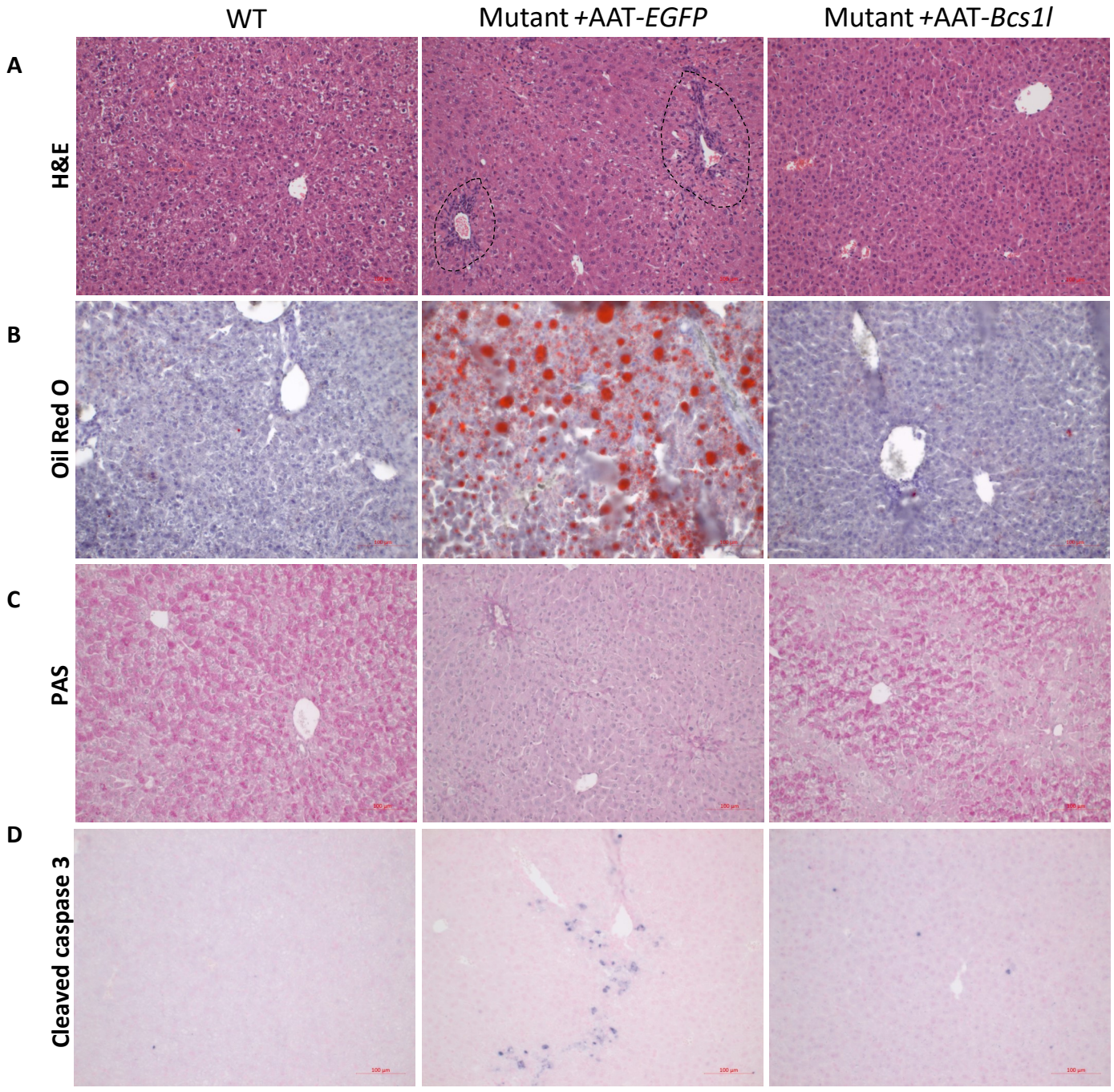
WT
Mutant +AAT-EGFP
Mutant +AAT-Bcs1l
A
H&E
B
Oil Red O
C
PAS
D
Cleaved caspase 3
100 µm

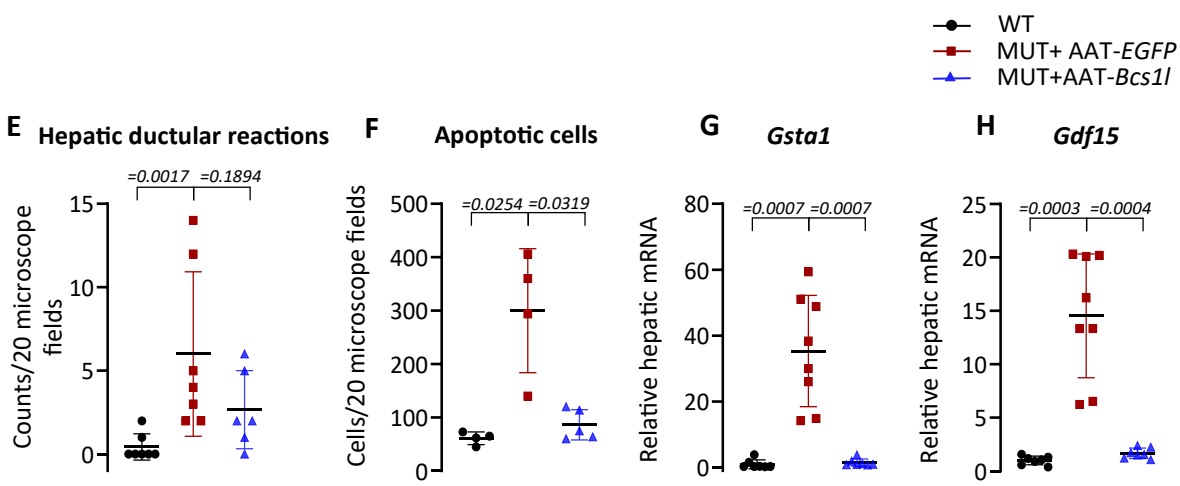
WT
MUT+ AAT-EGFP
MUT+AAT-Bcs1l
E
Hepatic ductular reactions
=0.0017
=0.1894
Counts/20 microscope fields
F
Apoptotic cells
=0.0254
=0.0319
Cells/20 microscope fields
G
Gsta1
=0.0007
=0.0007
Relative hepatic mRNA
H
Gdf15
=0.0003
=0.0004
Relative hepatic mRNA

Fig:3

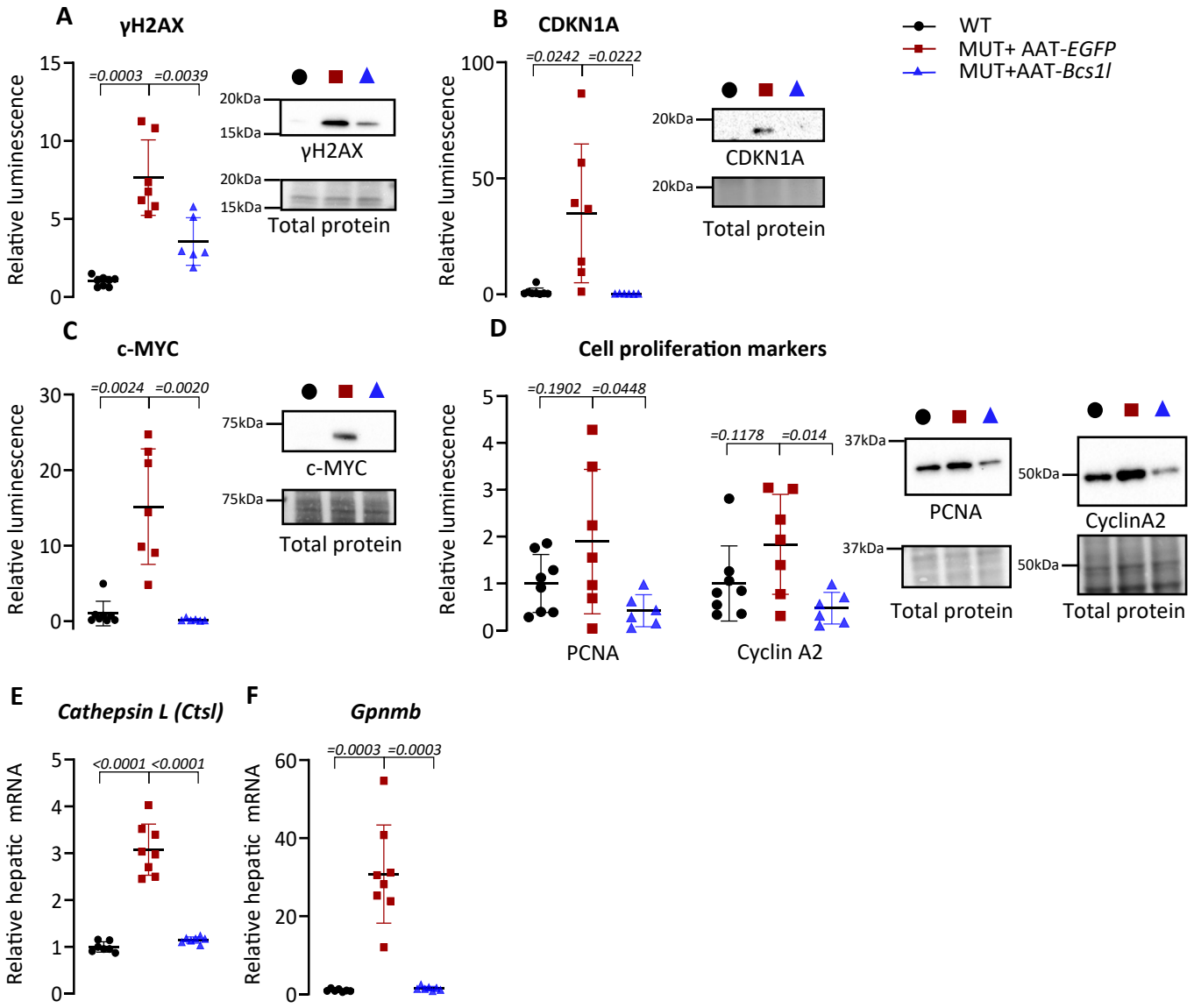
A
γH2AX
Relative luminescence
=0.0003
=0.0039
20kDa
15kDa
γH2AX
Total protein
B
CDKN1A
=0.0242
=0.0222
CDKN1A
Total protein
WT
MUT+ AAT-EGFP
MUT+AAT-Bcs1l
C
c-MYC
=0.0024
=0.0020
75kDa
c-MYC
Total protein
D
Cell proliferation markers
=0.1902
=0.0448
=0.1178
=0.014
37kDa
50kDa
PCNA
CyclinA2
Total protein
Cyclin A2
E
Cathepsin L (Ctsl)
Relative hepatic mRNA
<0.0001
<0.0001
F
Gpnmb
=0.0003
=0.0003

Fig:4

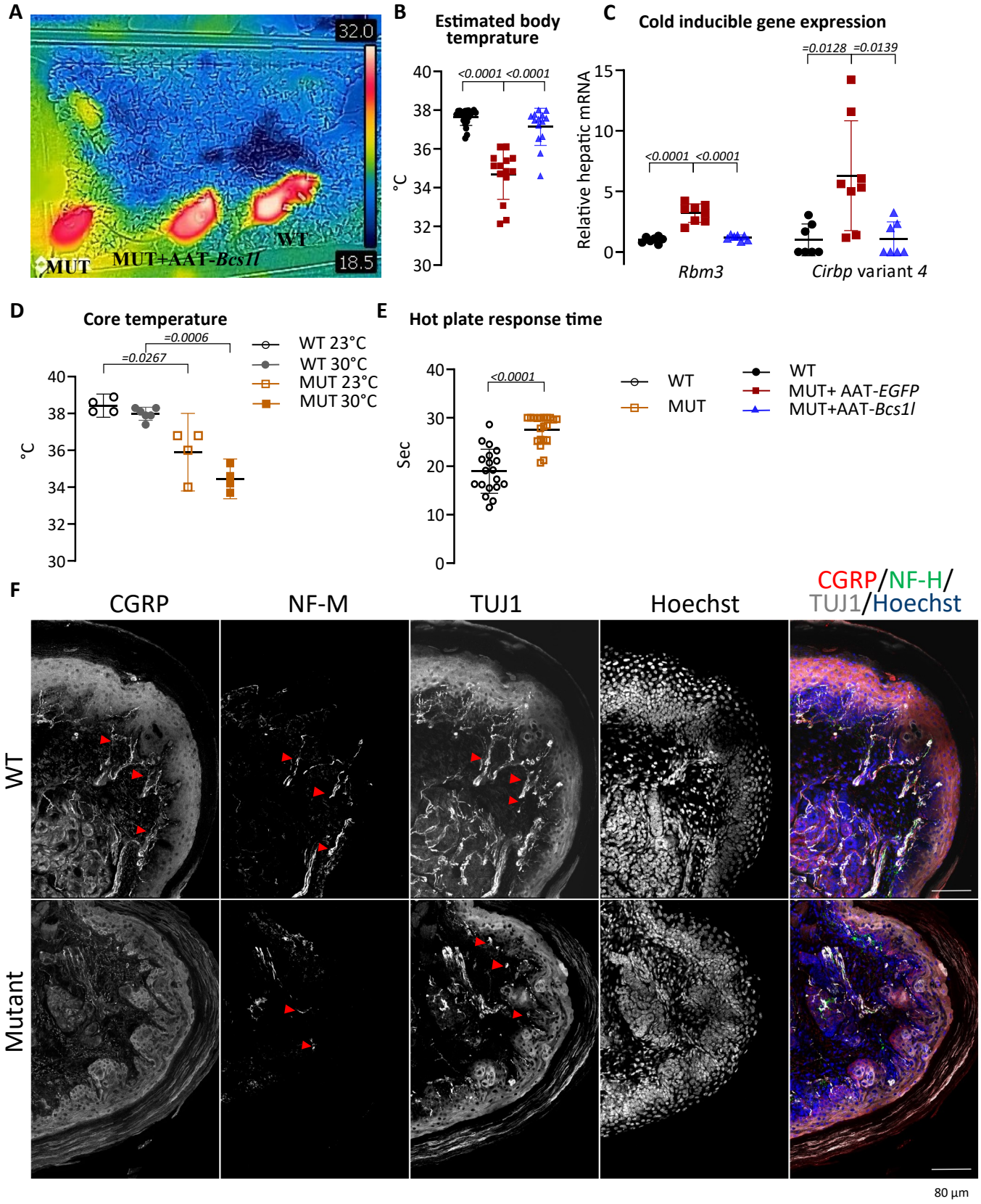
A
32.0
18.5
MUT
MUT+AAT-Bcs1l
WT
B
Estimated body temprature
°C
<0.0001 <0.0001
C
Cold inducible gene expression
Relative hepatic mRNA
<0.0001 <0.0001
=0.0128 =0.0139
Rbm3
Cirbp variant 4
D
Core temperature
°C
=0.0267
=0.0006
WT 23°C
WT 30°C
MUT 23°C
MUT 30°C
E
Hot plate response time
Sec
<0.0001
WT
MUT
WT
MUT+ AAT-EGFP
MUT+AAT-Bcs1l
F
CGRP
NF-M
TUJ1
Hoechst
CGRP/NF-H/
TUJ1/Hoechst
WT
Mutant
80 µm

Fig:5

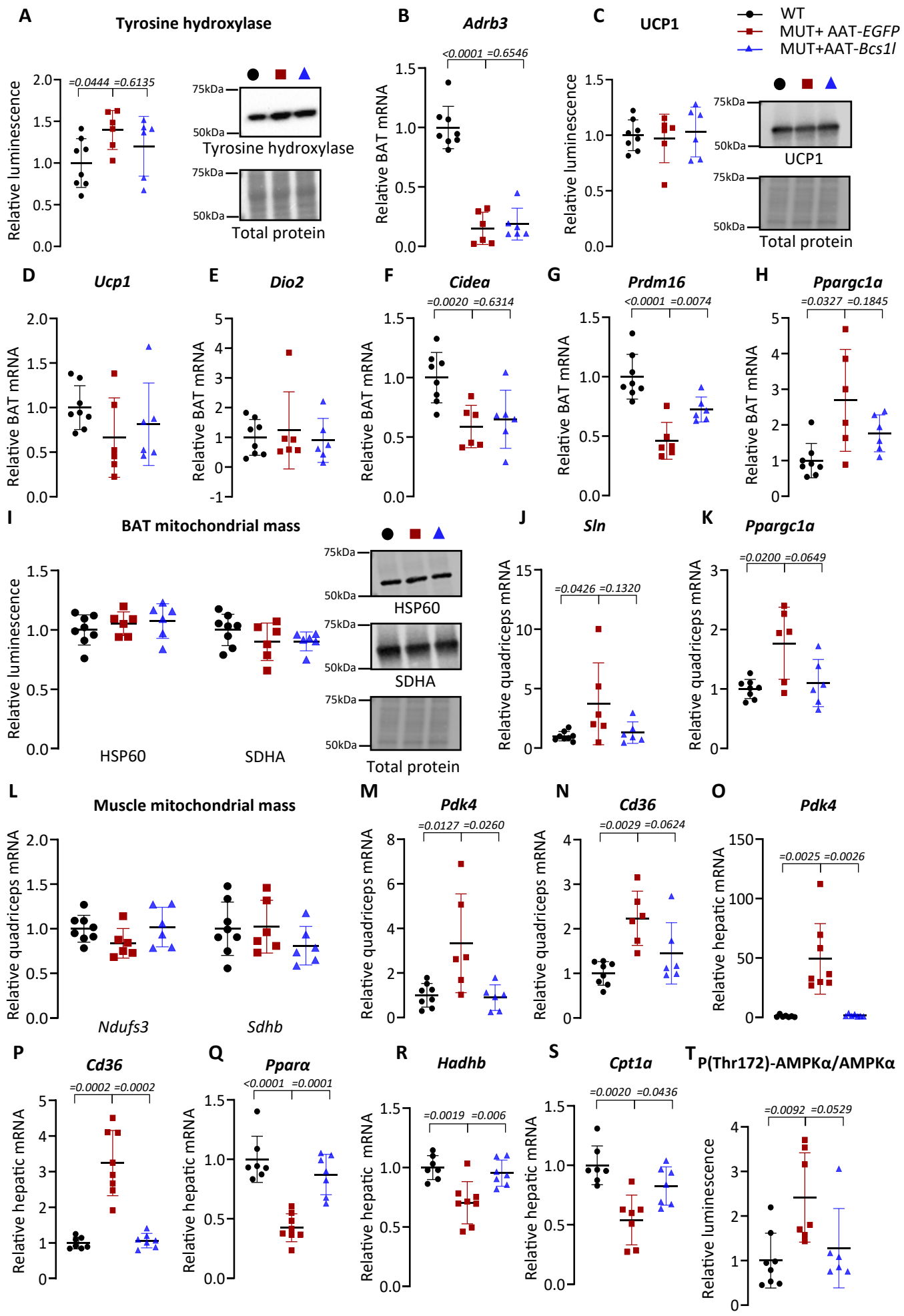
A
Tyrosine hydroxylase
Relative luminescence
=0.0444 =0.6135
75kDa
50kDa
Tyrosine hydroxylase
Total protein
B
Adrb3
Relative BAT mRNA
<0.0001 =0.6546
C
UCP1
Relative luminescence
UCP1
Total protein
WT
MUT+ AAT-EGFP
MUT+AAT-Bcs1l
D
Ucp1
E
Dio2
F
Cidea
=0.0020 =0.6314
G
Prdm16
<0.0001 =0.0074
H
Ppargc1a
=0.0327 =0.1845
I
BAT mitochondrial mass
HSP60
SDHA
J
Sln
Relative quadriceps mRNA
=0.0426 =0.1320
K
Ppargc1a
=0.0200 =0.0649
L
Muscle mitochondrial mass
Ndufs3
Sdhb
M
Pdk4
=0.0127 =0.0260
N
Cd36
=0.0029 =0.0624
O
Pdk4
Relative hepatic mRNA
=0.0025 =0.0026
P
Cd36
=0.0002 =0.0002
Q
Pparα
<0.0001 =0.0001
R
Hadhb
=0.0019 =0.006
S
Cpt1a
=0.0020 =0.0436
T
P(Thr172)-AMPKα/AMPKα
=0.0092 =0.0529

Fig:6

CIII-deficient mouse with compromised energy metabolism, and hypothermia

CIII-deficient mouse injected with rAAV-*Bcs1l* and hepatocyte respiration restored

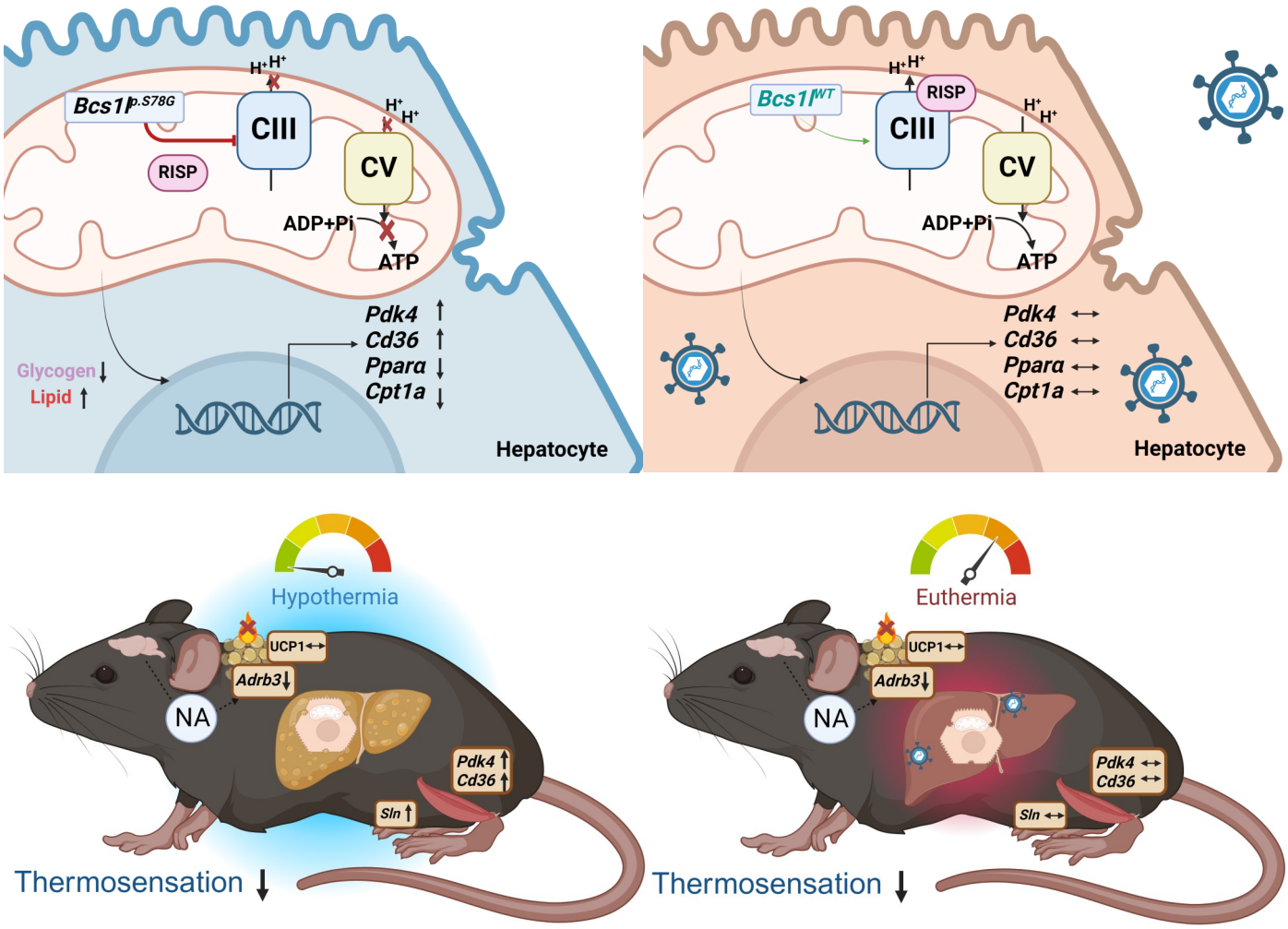

Fig:7

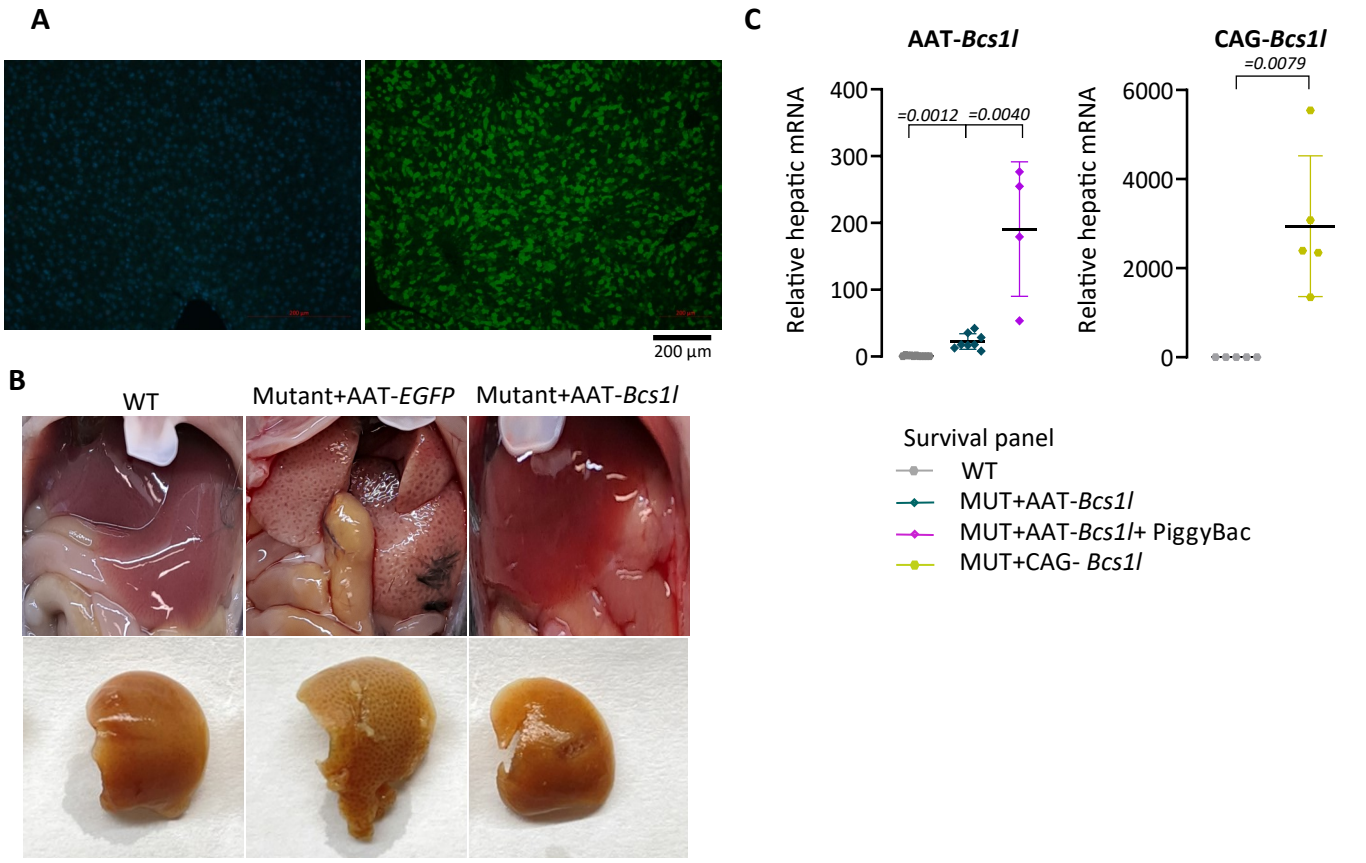
A
200 µm
B
WT
Mutant+AAT-EGFP
Mutant+AAT-Bcs1l
C
AAT-Bcs1l
Relative hepatic mRNA
400
300
200
100
0
=0.0012
=0.0040
CAG-Bcs1l
=0.0079
6000
4000
2000
0
Survival panel
WT
MUT+AAT-Bcs1l
MUT+AAT-Bcs1l+ PiggyBac
MUT+CAG- Bcs1l

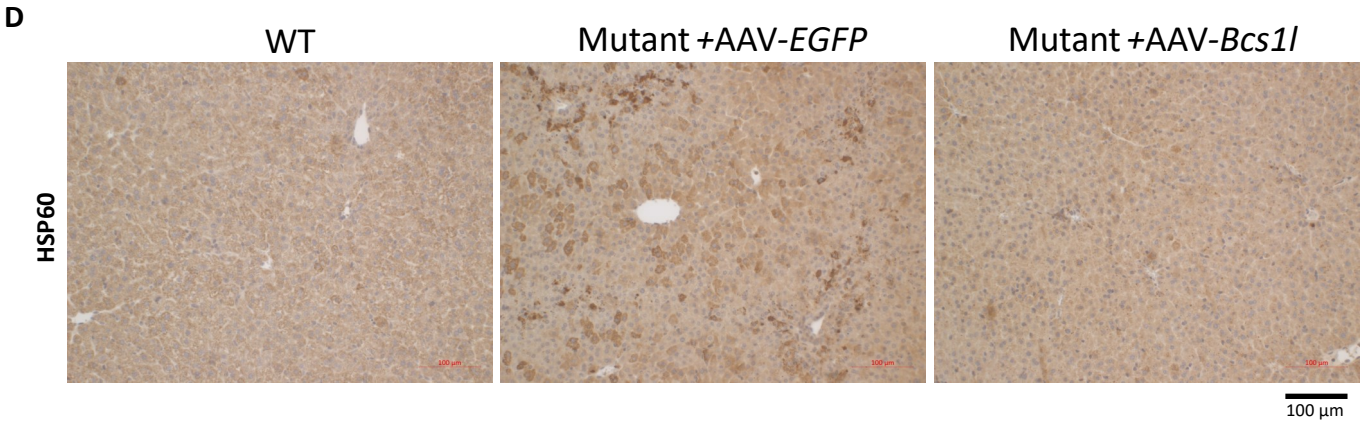
D
WT
Mutant +AAV-EGFP
Mutant +AAV-Bcs1l
HSP60
100 µm

Suppl. Fig:1

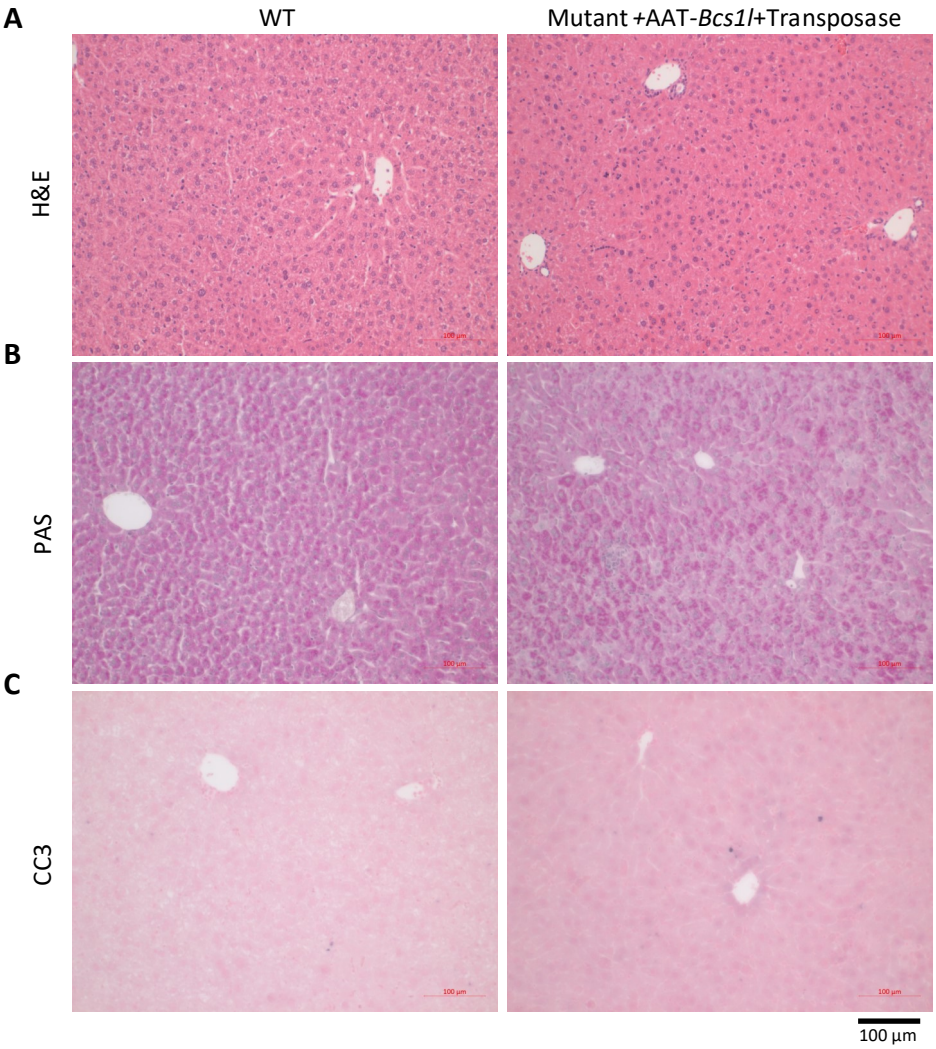
A
WT
Mutant +AAT-Bcs1l+Transposase
H&E
B
PAS
C
CC3
100 µm

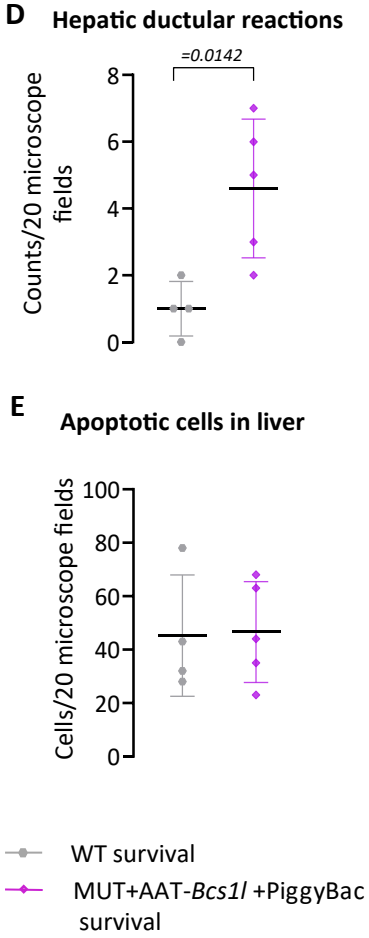
D
Hepatic ductular reactions
=0.0142
Counts/20 microscope fields
0
2
4
6
8
E
Apoptotic cells in liver
Cells/20 microscope fields
0
20
40
60
80
100
WT survival
MUT+AAT-Bcs1l +PiggyBac survival

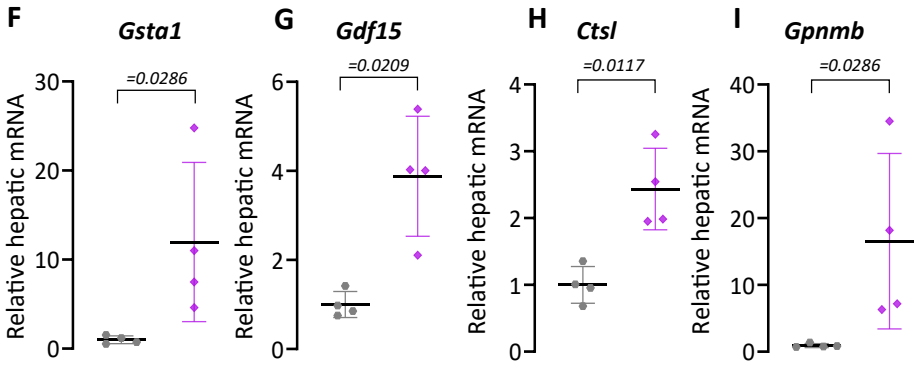
F
Gsta1
=0.0286
G
Gdf15
=0.0209
H
Ctsl
=0.0117
I
Gpnmb
=0.0286
Relative hepatic mRNA

Suppl. Fig:2

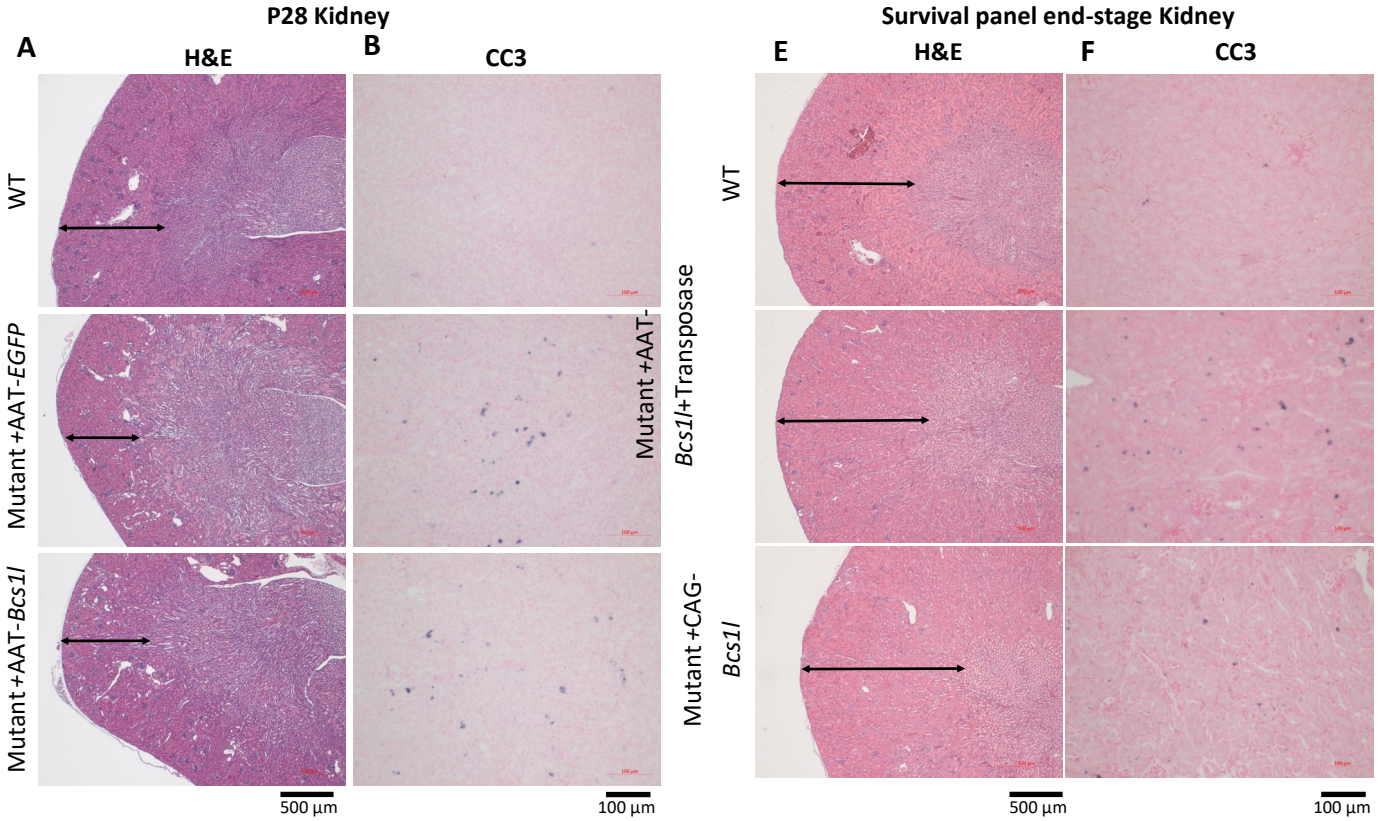

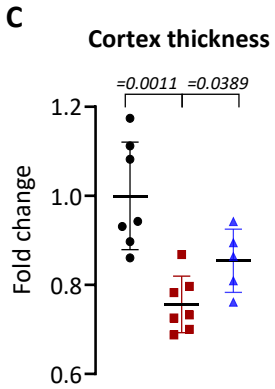

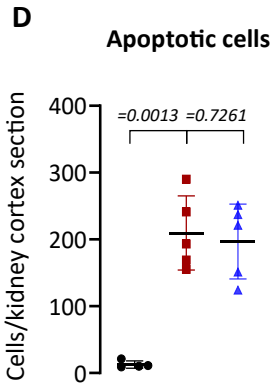

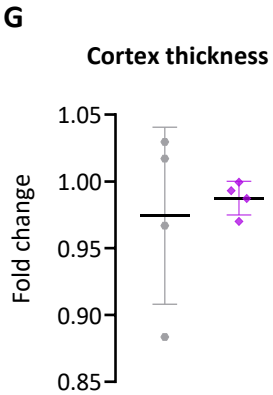

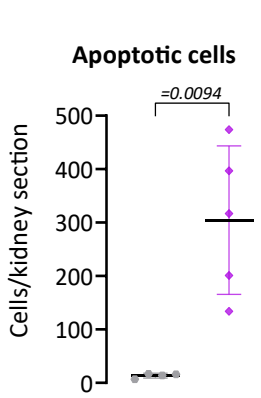

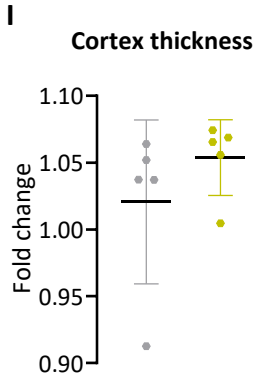

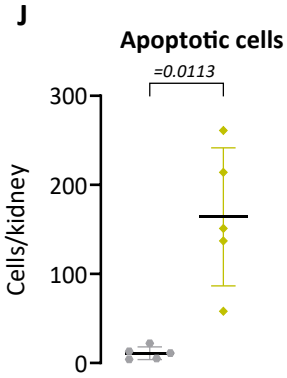

P28 panel
- WT
- MUT+ AAT-*EGFP*
- MUT+AAT-*Bcs1l*

Survival panel
- WT
- MUT+AAT-*Bcs1l*
- MUT+AAT-*Bcs1l*+ PiggyBac
- MUT+CAG- *Bcs1l*

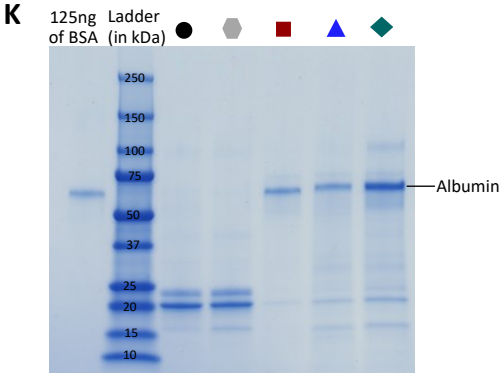

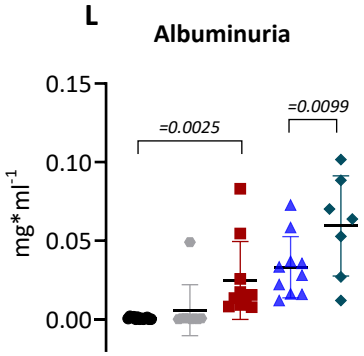

Suppl. Fig:3

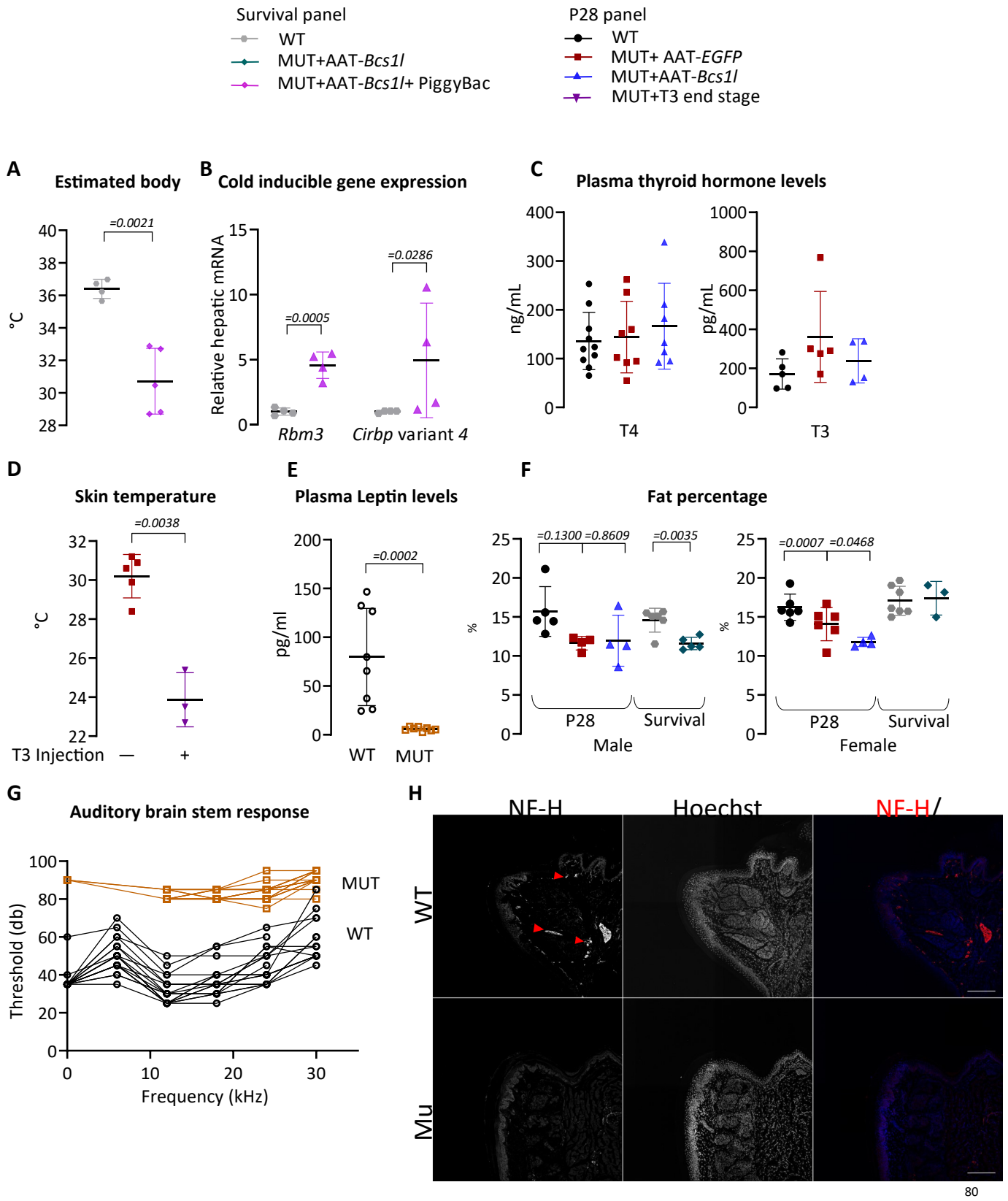
Survival panel
WT
MUT+AAT-Bcs1l
MUT+AAT-Bcs1l+ PiggyBac
P28 panel
WT
MUT+ AAT-EGFP
MUT+AAT-Bcs1l
MUT+T3 end stage
A
Estimated body
=0.0021
°C
B
Cold inducible gene expression
Relative hepatic mRNA
=0.0005
=0.0286
Rbm3
Cirbp variant 4
C
Plasma thyroid hormone levels
ng/mL
pg/mL
T4
T3
D
Skin temperature
=0.0038
°C
T3 Injection
—
+
E
Plasma Leptin levels
=0.0002
pg/ml
WT
MUT
F
Fat percentage
=0.1300 =0.8609
=0.0035
=0.0007 =0.0468
%
P28
Survival
Male
Female
G
Auditory brain stem response
Threshold (db)
Frequency (kHz)
MUT
WT
H
NF-H
Hoechst
NF-H/
WT
Mu

Suppl. Fig: 4

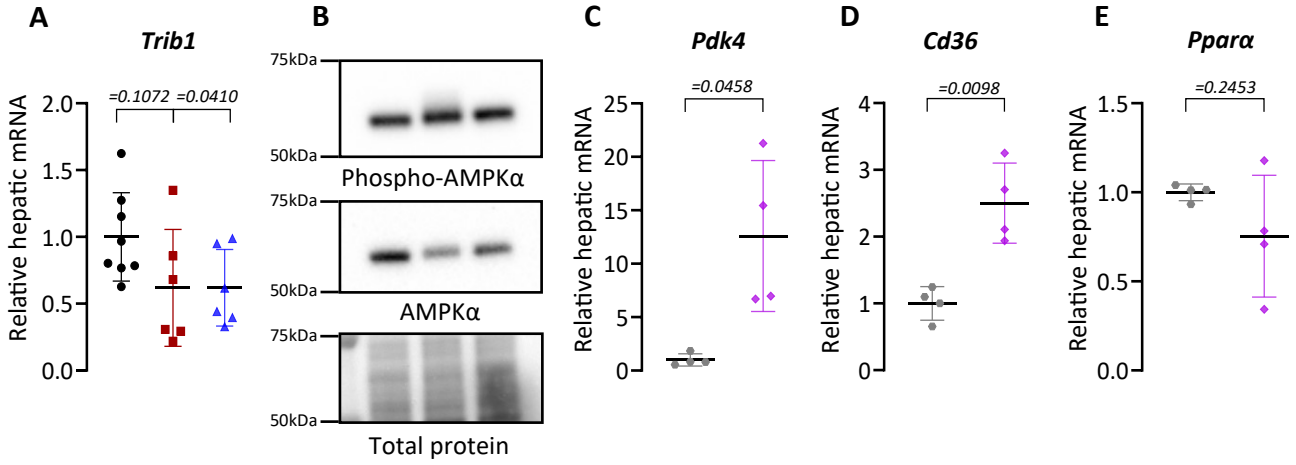
A
Trib1
Relative hepatic mRNA
2.0
1.5
1.0
0.5
0.0
=0.1072
=0.0410
B
75kDa
50kDa
Phospho-AMPKα
75kDa
50kDa
AMPKα
75kDa
50kDa
Total protein
C
Pdk4
Relative hepatic mRNA
25
20
15
10
5
0
=0.0458
D
Cd36
Relative hepatic mRNA
4
3
2
1
0
=0.0098
E
Pparα
Relative hepatic mRNA
1.5
1.0
0.5
0.0
=0.2453

Suppl. Fig: 5

Supplementary Table 1: Oligonucleotide sequences in 5' to 3' direction

qPCR primers	**Forward primer**	**Reverse primer**
AAT-*Bcs1l*	AGAACTAGTGGATCCCCCGG	CCACACCTACCAGCCCAAAT
Total *Bcs1l*	GATGTGGATGCTGCTTTTCTC	CGGCCTAGTCCTTGGTACTTT
CAG-*Bcs1l*	CCAGGTGCAAGGCTACTTCA	AGCAGCGTATCCACATAGCG
Igf1	AGCAGCCTTCCAACTCAATTAT	GAAGACGACATGATGTGTATCTTTATC
Ppargc1a	TGTGGAACTCTCTGGAACTGC	AGGGTTATCTTGGTTGGCTTTA
Gsta1	CTTCTGACCCCTTTCCCTCT	GCTGCCAGGCTGTAGGAAC
Gdf15	GTCTCCCCGAAGCCTACC	TTCAGGGGCCTAGTGATGTC
Areg	GCTGAGGACAATGCAGGGTAA	AGTGACAACTGGGCATCTGG
Bct	AATTCTCCACTGTGTGGTAGCA	GGTTTTCACTTTCTGTCTAGGGG
Ccl3	CCAGCCAGGTGTCATTTTCCTGA	GCTCAAGCCCCTGCTCTAC
Il1rn	GGCAGTGGAAGACCTTGTGT	CATCTTGCAGGGTCTTTTCC
Ctsl	CCCTATGAAGCGAAGGACGG	CTGGAGAGACGGATGGCTTG
Gpmnb	AAAATTGCTGACCACTTAGGACA	TCTCCAAACATTGCCAAACA
Cd36	GAACCACTGCTTTCAAAAACTGG	TGCTGTTCTTTGCCACGTCA
Cpt1a	CTCCGCCTGAGCCATGAAG	CACCAGTGATGATGCCATTCT
Pparα	GGGACTGCCAGTAAGCTATCC	CTTTGAAGCCAAGGCCACT
Hadhb	ACTACATCAAAATGGGCTCTCAG	AGCAGAAATGGAATGCGGACC
Lipc	ATGGGAAATCCCCTCCAAATCT	GTGCTGAGGTCTGAGACGA
Pdk4	GAGAGAGGGAAGCAAGAAAGGA	GAGACCCACAGAAGAAGCCATA
Srebp1	GATGTGCGAACTGGACACAG	CATAGGGGGCGTCAAACAG
Ucp1	AGGCTTCCAGTACCATTAGGT	CTGAGTGAGGCAAAGCTGATTT
β3ar	CCTTCCGTCGTCTTCTGTGT	CAGCTTCCTTGCTGGATCTT
Sln	GCTCCTCTTCAGGAAGTGAAG	TGGCCCCTCAGTATTGGTAGG
Ndufs3	AAGCAGCTCTCAGCATTTGG	ACTCATCAAGGCAGGACACC
Sdhb	CTGGTGGAACGGAGACAAGT	GCGTTCCTCTGTGAAGTCGT
Gak	CTGCCCACCAGGCATTTG	CCATGTCACATACATATTCAATGTACCT
Rab11a	AAGGCACAGATATGGGACACA	CCTACTGCTCCACGATAGTATGC
Rbm3	ACCGATGAACAGGCACTTGAA	ATGCTCTGGGTTTGTGAAGGT
Cirbpv4	GGGGTCCTGGCATTCTTCTC	GCTGAGTCCTCCCACGAAAA
Trib1	AGAACCCAGCTTAGACTGGAA	AAAAGCGTATAGAGCATCACCC
Dio2	GGGGTCCTGGCATTCTTCTC	GCTGAGTCCTCCCACGAAAA
Cidea	ATCACAACTGGCCTGGTTACG	TACTACCCGGTGTCCATTTCT
Prdm16	CCACCAGCGAGGACTTCAC	GGAGGACTCTCGTAGCTCGAA

Supplementary Table 2: Antibodies

Target	Antibody type	Source	Identifier	Dilution in WB
CDKN1A	Rabbit monoclonal	Abcam	Clone EPR18021, ab188224	0.25 µg/ml
γH2AX	Rabbit monoclonal	Abcam	Clone EP854(2)Y, ab81299	70 ng/ml
VDAC1	Mouse monoclonal	Abcam	clone 20B12AF2, ab14734	0.2 µg/ml
c-MYC	Rabbit monoclonal	Abcam	Clone Y69, ab32072	0.1 µg/ml
P(Thr172)-AMPKα	Rabbit monoclonal	Cell Signaling Technology	Clone 40H9, 2535	1:4000
AMPKα	Rabbit monoclonal	Cell Signaling Technology	Clone 23A3, 2603	1:2000
PCNA	Mouse monoclonal	Dako	Clone PC10, M0879	1:3000
Cyclin A2	Rabbit monoclonal	Abcam	Clone EPR17351, ab181591	0.125 µg/ml
HSP60	Rabbit polyclonal	Invitrogen	PA5-79414	0.125 µg/ml
UCP1	Rabbit polyclonal	Abcam	Clone SLC25A7, ab23841	1:2000
SDHA	Mouse monoclonal	Abcam	Clone 2E3GC12FB2AE2, ab14715	0.2 µg/ml
Tyrosine Hydroxylase	Rabbit polyclonal	Novus Biologics	NB300-109	1:1500
Rabbit IgG	Goat polyclonal, peroxidase conjugate	Cell Signaling Technology	7074	1:2000-1:4000
Mouse IgG	Goat polyclonal, peroxidase conjugate	Cell Signaling Technology	7076	1:2000-1:4000

Target	**Antibody type**	**Source**	**Identifier**	**Dilution in ICC**
HSP60	Rabbit polyclonal	Invitrogen	PA5-79414	0.5 µg/ml
γH2AX	Rabbit monoclonal	Cell Signaling Technology	Clone (Asp175), 9661	1:400
Target	**Antibody type**	**Source**	**Identifier**	**Dilution in IF**
TUJ1	Rabbit polyclonal	Abcam	AB18207	1:500
NF-M	Mouse monoclonal	Invitrogen	RMO-270	1 ng/ml
CGRP	Goat polyclonal	Abcam	ab36001	12.5 µg/ml
NF-H	Chicken polyclonal	Abcam	AB72996	1:1000
Goat anti-Chicken IgY (H+L) Cross-Adsorbed Secondary Antibody, Alexa Fluor™ Plus 488	Goat polyclonal	Thermo Fisher	A32931	1:400
Alexa Fluor® 488 AffiniPure™ Donkey Anti-Goat IgG (H+L)	Donkey polyclonal	Jackson ImmunoResearch	705-546-147	1:400
Donkey anti-Mouse IgG (H+L) Alexa Fluor™ 568	Donkey polyclonal	Thermo Fisher	A10037	1:400
Donkey anti-Rabbit IgG (H+L) Alexa Fluor™ Plus 647	Donkey polyclonal	Thermo Fisher	A32795	1:400